



Model-simulated hydroclimate variability of the East Asian Summer Monsoon across different climates: insights from a moisture source perspective

Astrid Fremme¹⁺, Paul Hezel^{1*}, Øyvind Seland², and Harald Sodemann¹

¹Geophysical Institute, University of Bergen, and Bjerknes Centre for Climate Research, Bergen, Norway

²Meteorologisk Institutt, Blindern, Norway

*Now at: Alfred Wegener Institute, Helmholtz Centre for Polar and Marine Research, Potsdam, Germany

+Now at: Statkraft, Norway

Correspondence: Harald Sodemann (harald.sodemann@uib.no)

Abstract. Here we study the sensitivity of monsoon season precipitation in the Yangtse River Valley (YRV, 110-122° E and 27-33° N, East China) to climatic boundary conditions from the last glacial maximum (LGM), pre-industrial conditions, and with the RCP6.0 emission scenario. Using a quantitative Lagrangian moisture source diagnostic, we interpret changes in precipitation amount and seasonality in terms of processes at the source regions that contribute to YRV precipitation. Thereby, we gain insight into influential processes and characteristics related to precipitation variability, and the sensitivity of the summer monsoon hydroclimate in East Asia to boundary condition changes in models. Comparing 10-year time slices similar to present-day conditions from the NorESM1-M and CAM5.1 models to ERA Interim reanalysis data reveals overall very similar moisture source regions, albeit with a tendency to more local precipitation origin in the climate models. Also across different climate forcings, the general characteristics of the moisture sources and moisture transport to the YRV are relatively stable, both concerning the location of source regions, their magnitudes, and the relative contributions of moisture from land and ocean areas. Differences in moisture source conditions are larger between the different climate models, than between different climatic boundary conditions using the same model. Overall, these findings imply that the moisture source regions, and thus the general processes of precipitation in the YRV could remain relatively stable across different climatic periods. However, the results may also indicate that current climate models underestimate the potential for non-linear responses to changing boundary conditions. The plausibility of moisture source changes simulated by the different models could in be evaluated in the future using paleoclimatic records, such as the stable isotope composition in cave sediments. Overall, our findings underline that the diagnosis of moisture sources provides a useful additional perspective for understanding and quantifying precipitation mechanisms and the hydroclimate simulated by models.

1 Introduction

Hydroclimate variability is intimately linked to climate variations on inter-annual to millennial time scales. Climate, and in particular hydroclimate variability in the East Asian summer monsoon (EASM) region, is of wider interest, as changes in this system can have important consequences for other parts of the world climate. Furthermore, the livelihood of a large population



is adapted on the present climatic conditions in this region (Zong and Chen, 2000). In light of such relevance of monsoonal variability, paleoclimate archives in East Asia have been pivotal for the general understanding of monsoon systems, and their variability on long time scales (Thompson et al., 2000; Wang et al., 2001; Dykoski et al., 2005; Hu et al., 2008; Wang et al., 2017). However, the complex interaction of land, ocean, topography, and atmospheric dynamics in this region render the identification of mechanisms that underly precipitation changes challenging. Here, we use a robust diagnostic for precipitation sources and transport to understand by which mechanisms general circulation models (GCMs) hydroclimate variability in the EASM region across different climatic conditions.

Simulating the hydroclimate in the global monsoon regions has been notoriously challenging, both for past and present climates. In addition to variability on different time scales, climate models struggle to reproduce the spatial details of precipitation and other relevant variables (Braconnot et al., 2012). For example, a weaker meridional temperature gradient in the troposphere, arising from the differential heating over the Tibetan Himalayas and the Indian Ocean, leads in many models to a later onset and weaker monsoon circulation with less precipitation (Ashfaq et al., 2017). A major reason for model deficiencies clearly lies in the limited horizontal resolution in common GCMs, which requires a large share of processes to be handled by sub-grid scale parameterisations. Furthermore, the complex interplay of physical and dynamical factors is often represented poorly, including convection, low-level jets, topography, and land-surface processes (Webster et al., 1998; Hoyos and Webster, 2007; Seo et al., 2013). Hydroclimate variability may be particularly sensitive to such interplay of different factors, as the atmospheric water cycle is connected to the land and ocean surface by surface fluxes and precipitation, leading to precipitation recycling (Fremme and Sodemann, 2019; Gimeno et al., 2021). Since water vapour is a central feedback mechanism of the climate system, better understanding by which mechanisms the hydroclimate in GCMs forms can benefit climate model development.

Small-scale variability of precipitation in space and time, both in observations and simulations, renders precipitation a particularly challenging variable for studying processes contributing to hydroclimate variability. While precipitation is a key target variable of climate models, its representation in the grid-scale microphysics and in moist convection parameterisations differ markedly between models. In this context, more robust means than precipitation fields for evaluating the hydroclimate across different models can therefore be a valuable addition to evaluation studies. The horizontal moisture flux, expressed as integrated vapor transport, has been shown to be associated with higher predictability than precipitation, specifically for precipitation extremes (Lavers and Villarini, 2013). Horizontal moisture flux and integrated vapour transport can be visualised effectively by mapping the evaporation sources corresponding to precipitation, often referred to as the moisture sources (Stohl et al., 2008; Bohlinger et al., 2017; Fremme and Sodemann, 2019). We hypothesize that by combining diagnosed moisture sources, moisture transport and precipitation in simulations allows to identify causal links behind hydroclimatic variability more readily than by considering precipitation directly.

Stable isotope parameters, such as $\delta^{18}O$ in carbonates, ice cores, and tree rings have commonly been interpreted as monsoon strength or monsoon precipitation intensity, thus reflecting regional precipitation amount (Wang et al., 2001). However, some studies show that the isotopic information stored in these records may at times be influenced or even dominated by other effects, such as circulation-induced moisture source changes (Maher and Thompson, 2012). Changes in land surface parameters are a further factor that has not yet been thoroughly explored, but could potentially play an important role (Fremme and



Sodemann, 2019). Adopting a moisture source perspective has been shown to be potentially valuable for interpreting the paleoclimate information contained in stable water isotopes from different archives in the East Asian Monsoon region using reanalysis data (Liu et al., 2014; Baker et al., 2015). Insight into what consequences model-simulated hydroclimate variability for different climates has with regard to moisture source changes, and thus both evaporation conditions and atmospheric transport conditions, could therefore be also be highly beneficial for the interpretation of paleoclimate records, and provide ground truth for model-simulated hydroclimate.

Previous studies that investigated the contribution for land and ocean areas as moisture sources to the EASM region differ markedly in their results. The most important oceanic source regions appear to be the Arabian Sea, the Bay of Bengal, the South China Sea, and the Western Pacific (Wei et al., 2012; Wang et al., 2018), with southwesterly moisture transport providing a large fraction of the water vapor for the East Asian monsoon. While some authors emphasize the importance of oceanic regions over land areas ((Zhou and Yu, 2005; Chen et al., 2013)), several authors also have identified that land areas contribute substantial amounts (Wei et al., 2012; Sun and Wang, 2015). It appears that quantification of contributions from different source areas is strongly influenced by the respective methods. In a study based on ERA-Interim reanalysis data, Fremme and Sodemann (2019) analyzed the processes leading to seasonal and interannual variability of the Yangtze River Valley (YRV) precipitation variability using a Lagrangian moisture source and transport diagnostic that determines source regions without the need to pre-specify the atmospheric lifetime of water vapour (Sodemann, 2020). Based on the quantification of moisture sources for the period 1980–2016, the study of Fremme and Sodemann (2019) revealed a major role of land surface processes, leading to several cycles of precipitation recycling for 50-65 % of the rainfall in the YRV. Since previous studies mapping the moisture sources for precipitation in East China only covered recent periods, moisture source changes across different climates, and in particular the respective role of land contributions, have so far not been assessed with such a method.

Here we use the Lagrangian moisture source diagnostic of Sodemann et al. (2008) to obtain the moisture sources of the YRV as a core region of the East Asian monsoon system using simulations from two climate models for different climatic periods. This is the first time this moisture diagnostic is used with free-running model simulations without influences from data assimilation associated with reanalysis data. First, we assess how different climate models transport moisture to the YRV during the monsoon season in a present-day climate, using results obtained previously from reanalyses as a reference (Fremme and Sodemann, 2019). From simulations with different climatic boundary conditions, we then identify how models represent hydroclimate variability during the simulated East Asian Summer monsoon to orbital forcing and ice-sheet topography from analyzing time slices of an uncoupled simulation of the last glacial maximum (LGM). Furthermore, the changes of the monsoon system in a future climate scenario with increased atmospheric CO₂ concentrations are assessed in a coupled model run for a time slice near end of the 21st century. Based on our findings, we then discuss in particular the role of land-surface processes, and conclude with remarks on the potential of a moisture source perspective for understanding hydroclimate variability, and for interpreting paleoclimate records from the East-Asian monsoon region.



90 2 Methods and Data

The aim of our study is to investigate the response of the hydroclimate to different climate model configurations for the East Asian monsoon from a moisture source perspective. As in the study of Fremme and Sodemann (2019), we use the YRV as a focus region, defined here as the lower reaches of the Yangtze River 110–122° E and 27–33° N, East China. We apply the widely used quantitative Lagrangian moisture source and transport diagnostic by Sodemann et al. (2008) based on FLEXPART (Flexible Particle Transport Model, (Stohl et al., 2005)) backward particle trajectories to find the moisture sources of the YRV in different climate model simulations and time slices. We first describe the setup of the climate model simulations, followed by an explanation of the trajectory calculation setup, and a description of the moisture source diagnostics based on climate model data.

2.1 Climate model simulations

100 In total we analyze moisture transport and sources for the YRV in four climate model simulations, contributed by two different climate models (Fig. 1a, Table 1). The two models are the atmosphere-only Community Atmosphere Model CAM5.1 (Neale et al., 2012), and the fully coupled ocean-atmosphere Norwegian Earth System Model (NorESM1-M; Bentsen et al., 2013). For each model, we analyse a control simulation for present climate conditions to assess how precipitation is represented in comparison to reanalysis data, and one simulation of a different climate (Fig. 1a). For the uncoupled, atmosphere-only simulations with CAM5.1, we analyze a simulation of the preindustrial period (PIN) as reference, and then evaluate the sensitivity by comparing to a simulation of the Last Glacial Maximum (LGM) climate. For the coupled ocean-atmosphere simulations with NorESM1-M, a time slice from a control run with present-day conditions (CTL) is used as reference, and time slice from a transient simulation with the CMIP5 Representative Concentration Pathway (RCP) 6.0 emission scenario (RCP) allows to assess sensitivity to a future climate. By comparing moisture source results from reanalysis with the near present-day simulations, and the near present-day with a different climate from the corresponding model, these four model simulations enable an assessment of how models represent moisture source changes for changing climate conditions (Fig. 1a, arrows). For the calculation of trajectories and diagnosis of moisture sources, it was necessary to output and archive 3-dimensional model fields of wind, temperature and humidity were required at a 3-hour time interval (Cassiani et al., 2016). This requirement poses severe limitations on the duration and number of simulations that can be performed and archived over longer time.

115 The two atmosphere-only CAM5.1 simulations PIN and LGM were run with a resolution of $0.9 \times 1.25^\circ$, with 30 vertical levels, using the finite-volume dynamical core (Neale et al., 2012). Both simulations were run for 30 years each, starting after a 3-year spinup period (Table 1). The PIN simulation used climatological SSTs and sea ice from the merged Hadley-NOAA/OI Sea Surface Temperature and Sea-Ice Concentration dataset (Hurrell et al., 2013), averaged for the period of 1870–1899. Atmospheric carbon dioxide was prescribed at a mixing ratio 284.7 ppmv, and atmospheric methane at a mixing ratio of 791.6 ppbv. 120 The LGM simulation used the topography and ice sheets specified as in PMIP3 (Braconnot et al., 2012; Abe-Ouchi et al., 2015) and CMIP5 (Taylor et al., 2012) experiments for 21 kya. LGM SSTs and sea ice climatology were obtained from 21 kya simulations performed at NCAR for the LGM (<https://www.earthsystemgrid.org/dataset/ucar.cgd.cesm4.b40.lgm21ka.1deg.003M>).

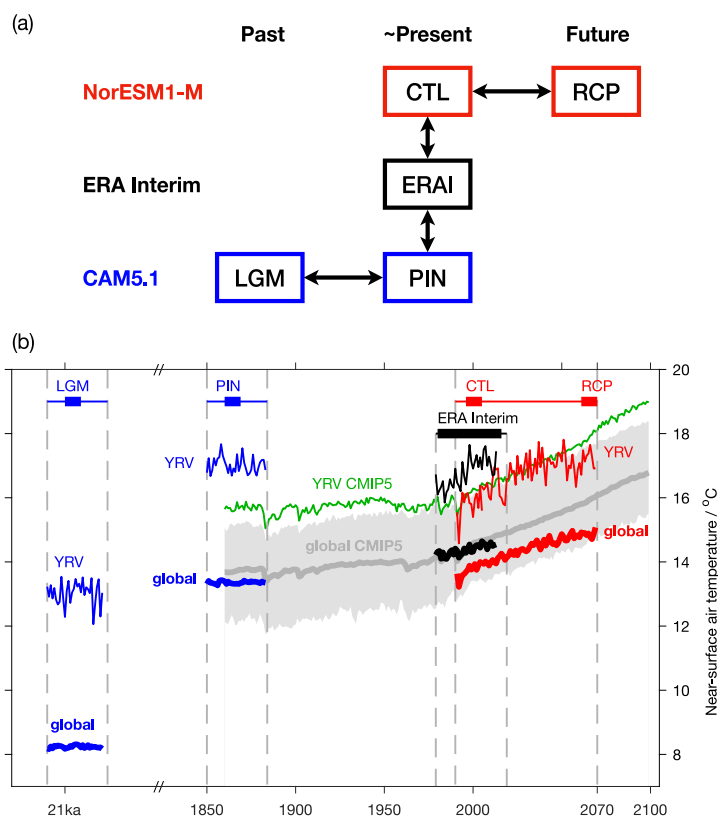


Figure 1. Overview of the study set-up. (a) Schematic for the comparison between the simulations with NorESM1-M (red) for near-present (Control, CTL) and a future climate (Reference Climate Projection 6.0, RCP), with CAM5.1 (blue) for near-present (Pre-Industrial, PIN) and a past climate (Last Glacial Maximum, LGM), and the reference present-day climate from ERA-Interim (ERA Interim, black). (b) Compilation of near-surface temperatures from all datasets for global mean (thick lines) and the Yangtse River Valley (thin lines). Global mean and spread of near-surface temperatures from the CMIP5 multi-model mean for RCP6.0 from 1860 to 2075 (Taylor et al., 2012) are shown in grey, and green line shows the mean for the YRV domain. The duration of simulations with CAM5.1 and NorESM1-M are shown with blue and thin lines red lines on top. Thick blue lines show the years for which moisture sources have been analyzed. Note the broken time axis between 1850 and 21 thousand years ago (21ka).

html). Sea level was kept at PIN conditions during the LGM simulations, potentially introducing unrealistic land-atmosphere interaction in the region of the Maritime continent and West Pacific Warm Pool region. Mixing ratios of atmospheric greenhouse gases were 185 ppmv for CO₂, and 185 ppmv for methane during the LGM simulation. In the YRV region, temperatures are simulated to be on average 13.0 °C, which is 4.8 K warmer than the global average of 8.2 °C (Fig. 1b, thick and thin blue lines). This global average LGM temperature change is larger than estimates from reconstructions (4.0 K, Annan and Hargreaves, 2013). During PIN, in comparison, the global mean screen-level temperature is 13.4 °C, which is 3.6 K colder than in the YRV (17.0 °C).



130 The coupled NorESM1-M simulations CTL and RCP had a horizontal resolution of $1.88^{\circ} \times 2.50^{\circ}$ with 26 vertical levels, and were run as a continuous simulation for a 80-year period from 1990–2070 (Table 1). NorESM1-M is based on CCSM version 4 (Gent et al., 2011), with the atmospheric component being CAM4-Oslo (Kirkevåg et al., 2013) and the CLM4 land component (Lawrence et al., 2011). In these simulations, greenhouse gases (CO_2 , CH_4 , N_2O , CFC-11 and CFC-12), volcanic SO_4 , total solar irradiance and the ozone distribution were prescribed for the historical period (Lamarque et al., 2010), and simulated
135 from 2005 onwards (Stohl et al., 2015). The climate simulations with NorESM1-M are separated into a control simulation (CTL) for present-day, and a future climate simulation (RCP). The global average screen-level temperature between CTL and RCP increase by 0.7 K for the RCP6.0 scenario, from 13.7 to 14.5 °C. NorESM1-M is thereby near the lower end of the range of climate model simulations contributed to CMIP5 (Fig. 1b, grey shading). In the YRV region, the temperature difference between CTL and RCP is 1.1 K. Notably, during CTL, the YRV region is only 2.1 K warmer than the global average, and 2.4 K
140 during RCP. Here, there is quite close agreement with the CMIP5 mean (Fig. 1b, green line).

For the observational period, both PIN and CTL model simulations are substantially colder than ERA-Interim (14.4 °C globally, and 16.8 in the YRV). A general cold bias over land in NorESM has been documented earlier (Seland, 2020, their Fig. 14), and could be related to aerosol properties; the ultimate reason remains however unknown. Clearly, some differences are always expected, as denoted by the spread of the CMIP5 models, and may be due to differences in the boundary conditions,
145 model resolution, atmospheric dynamics, physics parameterisations, and ocean model. We will return to some of the differences noted here when discussing the moisture source results.

2.2 Setup for moisture source analysis

The moisture sources for each climate model simulation were identified using the Lagrangian moisture source diagnostic WaterSip (Sodemann et al., 2008). The diagnostic identifies the evaporation sources and transport pathways of precipitation falling
150 in a target domain from specific humidity changes along backward trajectories. A particular advantage of this offline method is that it can be applied to meteorological fields and trajectories from different sources. Here, we calculated backward trajectories from the FLEXible PARTicle trajectory model (FLEXPART; Stohl et al., 2005; Pisso et al., 2019), using FLEXPART-NorESM/CAM (V1) (Cassiani et al., 2016) for the 3-hourly model level output from the climate models NorESM1-M and CAM5.1. This is the first use of the moisture source diagnostic with climate model output data.

155 For the FLEXPART setup, 50'000 air parcels of equal mass ($\sim 4.54 \times 10^{11}$ kg per parcel) in PIN and LGM, and 25'000 air parcels of equal mass ($\sim 1.15 \times 10^{12}$ kg per parcel) in CTL and RCP were initiated in the atmosphere over the YRV region ($108\text{--}124^{\circ}$ E and $25\text{--}35^{\circ}$ N). By means of the so-called domain-filling mode, FLEXPART constantly released new particles in proportion to the mass flux into the domain. Using 3-hourly, three-dimensional climate model output of wind, temperature and humidity, FLEXPART-NorESM/CAM then calculated air parcel movements backward for at least 16 days, starting from the
160 YRV domain defined above. Running for one time slice at a time, the FLEXPART model then stored air parcel trajectories including their horizontal and vertical position, air temperature, specific humidity, and surface characteristics at the position of each air parcel at a 3-hour time interval for use with the moisture source diagnostic WaterSip.



Due to computational and storage constraints, the trajectory calculation covered 10-year time slices for each climate model simulation (Table 1). For PIN and LGM, the 10-year periods were chosen such that the YRV precipitation mean was similar to that of the full simulation period. Due to the climatological SST forcing, the PIN and LGM simulations are not affected by ocean-induced inter-annual variability. The time slice for both the PIN and LGM time slice thus covered the model simulation years 0010-0019. For CTL, the latest 10-year period overlapping with the ERA-Interim period, and without a strong El Niño or La Niña was chosen (1996-2005). For the RCP time slice, we chose the 10-year period at the end of the future climate simulation (2061-2070).

2.3 Parameters for moisture source diagnostics

Next, the moisture source diagnostic WaterSip was used to evaluate the trajectories corresponding to each individual precipitation event in the YRV domain (for technical reasons here expanded to 110–122° E and 27–33° N). A particular advantage of the WaterSip method is that there is no need to pre-specify the life time of water vapour (Sodemann, 2020). However, several thresholds of the method need to be adapted when working with a new data source, such as our climate model output, to reliably identify moisture sources and their characteristics.

Evaluating each air parcel trajectory backward in time, specific humidity changes along the way provide an estimate of either a contribution of water vapour from surface evaporation to the air parcel, or the loss of water vapour due to precipitation along the way. Thereby, either evaporation or precipitation is assumed to dominate within a given time interval. Importantly, the contribution of surface evaporation at each moisture source is quantified relative to the water vapour already contained within an air parcel at a given time. Assuming well-mixed conditions within the air parcel (not within the column), all water vapour in the air parcel contributes to precipitation according to their relative share. Finally, the contribution of each individual source to total precipitation in the YRV is found from the precipitation amount-weighted integral of all trajectories within a given time interval. In addition to the sources' location, characteristics of the moisture sources and transport are identified, such as the moisture source distance, temperature, or surface type (see Sodemann et al., 2008; Fremme and Sodemann, 2019, for further details).

The WaterSip diagnostic was adapted to the target region and climate model input data used here by evaluating and adjusting several threshold parameters. Sensitivity to different time step lengths and thresholds for specific humidity changes (Δq_c) and relative humidity (RH_c) was assessed in detail for a sub-set of the data (Appendix A). Based on these sensitivity tests, the threshold for identifying significant changes in specific humidity per time step (Δq_c) was set to 0.1 g kg^{-1} at a 6 h^{-1} time step. Precipitating trajectories in the target region were identified from a relative humidity threshold ($RH_c > 80\%$).

We diagnosed the moisture transport for 15 days along each trajectory. No distinction between moisture sources identified near the surface, or within the free troposphere was made for this study. On average, the combination of parameter choices allows the WaterSip diagnostic tool to assign moisture sources to on about 95–98% of the precipitation estimated by the WaterSip diagnostic. This percentage is larger than usually obtained with trajectories from reanalysis data, possibly because of inconsistencies introduced during data assimilation.



Table 1. Characteristics of the four NorESM simulations and the ERA Interim reference.

Name	Description	Model	Grid resolution	Levels	Configuration	Years analyzed
PIN	Pre-Industrial (Control)	CAM5.1	1.25×0.94	30	prescribed ocean	0010-0014*
LGM	Last Glacial Maximum	CAM5.1	1.25×0.94	30	prescribed ocean	0010-0014*
RCP	IPCC's RCP6 scenario	NorESM1-M	2.50×1.88	26	fully coupled	2066-2070
CTL	Historical Control	NorESM1-M	2.50×1.88	26	fully coupled	2001-2005
ERA-Interim	ERA Interim reference	IFS	T255 (interpolated to 1.0×1.0)	61	prescribed ocean	1980-2016

*Model years.

2.4 Reference analysis

Since each climate model may have its own, model-specific representation of the hydrological cycle, we evaluate their performance using data from the European Centre for Medium-range Weather Forecast's (ECMWF) ERA-Interim reanalysis (Dee et al., 2011) as a reference. Several studies have shown that the ERA-Interim reanalysis provides a realistic representation of the climatic conditions in the YRV region (Lin et al., 2014; Huang et al., 2016).

We furthermore compare moisture sources from the climate models to the results of Fremme and Sodemann (2019). Fremme and Sodemann (2019) analysed YRV moisture sources based on ERA-Interim data and the WaterSip diagnostic from a global trajectory dataset (Läderach and Sodemann (2016)), spanning the period 1980–2016 (ERA-Interim; Table 1). The WaterSip parameters for the reanalysis climatology were the same as used here for the climate model simulations. In total, 95% of the estimated precipitation could be attributed to moisture sources in the reference analysis.

3 Results

Now, we first evaluate the performance of the climate model simulations in representing East Asian Monsoon precipitation. To this end, the near-present control simulations of CTL and PIN are compared to the reference climatology based on the ERA-Interim reanalysis (Fig. 1a, vertical column and arrows). Then, precipitation in the paleo-simulation (LGM) and in the future scenario simulation (RCP) are compared to precipitation from the corresponding control simulation from the same climate model.

3.1 Summer-time YRV precipitation in the near-present simulations PIN and CTL

In our analysis, we focus at the YRV summer monsoon precipitation, which peaks during May, June and July (MJJ). According to the ERA-Interim dataset, summer precipitation is at a maximum in a broad region between the Bay of Bengal and the southern border of the Tibetan Plateau (Fig. 2a). A distinct orographic precipitation gradient is apparent along the western edge of the Indian peninsula. A further precipitation maximum is apparent over the Philippines and Western Pacific as part of the

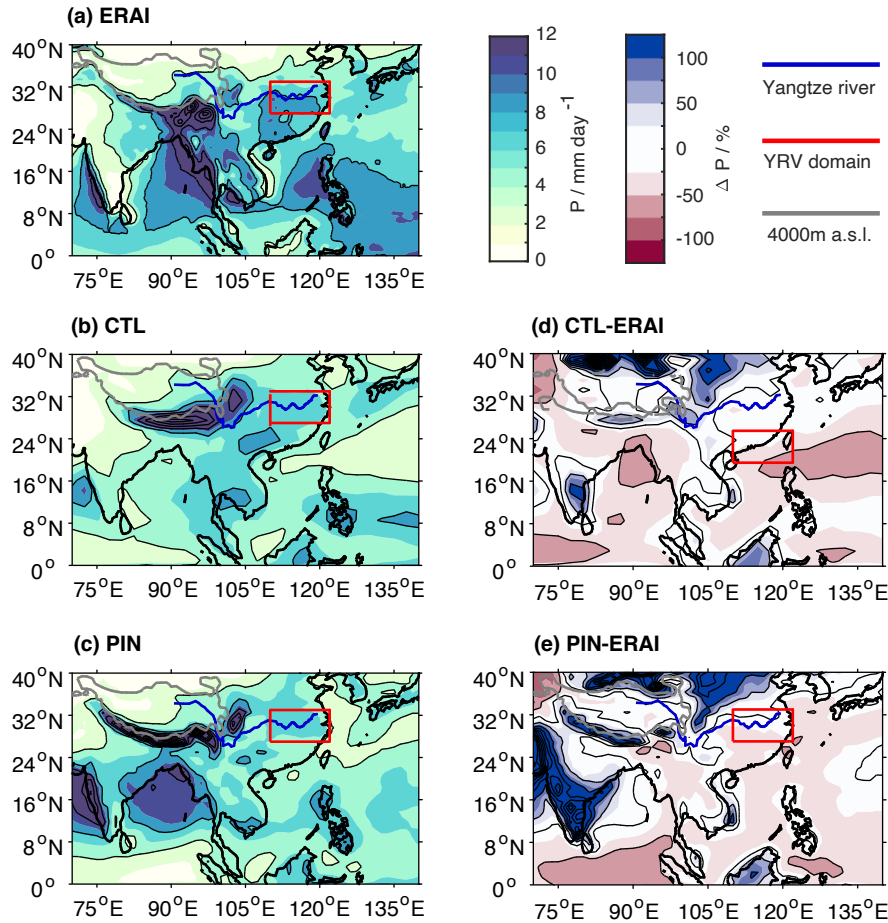


Figure 2. East Asian summer monsoon (MJJ) 10-year mean precipitation for (a) ERA Interim (2001-2010), (b) CTL (NorESM1-M, 2001-2009), (c) PIN (CAM5.1, 0010-0019) in mm day^{-1} (shading). Dashed precipitation contours are shown every 5 mm day^{-1} . Precipitation anomalies in comparison to ERA Interim are shown (d) for CTL-ERA and (e) the PIN-ERA (shading, %), with dashed contours every 50%. The YRV domain is outlined by a red box. The Yangtze river is denoted as a thick blue line, and elevation above 4000 m a.s.l. is indicated by a grey contour.

northwards displaced ITCZ. In the YRV region (Fig. 2a, red box), precipitation shows a relatively weak north-south gradient with average values of $5\text{--}9 \text{ mm day}^{-1}$ and with the highest values south and west within the region.

In comparison, the CTL simulation exhibits a similar range of precipitation values (Fig. 2b). The maximum along the southern edge of the Tibetan Plateau and western India are more spread out, and reach well above 12 mm day^{-1} . However, there is a clear lack of precipitation over the Bay of Bengal (BoB), and the Philippines. Precipitation underestimation seems to dominate in the CTL simulation for this region (Fig. 2d, red shading). Overestimation of precipitation is apparent to the southern edge of the Tibetan Plateau ($>100\%$ overestimation), southern India, and southeast Asia, which could in part occur



at the expense of the BoB precipitation. In the YRV, MJJ precipitation is between 10–50% lower than ERA-Interim. Here, the
225 CTL simulation has a precipitation range of 4–6 mm day⁻¹, clearly missing the finer details of spatial variability. Despite such
local biases, we at first order consider the CTL simulation to reasonably reproduce most of the large-scale features of summer
precipitation in East Asia when compared to the ERA-Interim reanalysis.

Similar precipitation characteristics as in the CTL simulation are present in the PIN model run (Fig. 2c). The precipitation
maximum along the southern edge of the Tibetan Plateau is more confined in the PIN run compared to CTL, but lacks the
230 maximum (≥ 12 mm day⁻¹) apparent over Bangladesh in ERA-Interim. The PIN simulation shows a more pronounced precipi-
tation maximum in the BoB compared to CTL (Fig. 2b). Over the YRV and large parts of the West Pacific, precipitation in
the PIN simulation is underestimated (Fig. 2e, red shading), exceeding 50% to the southeast of YRV. In that region, the PIN
simulation (Fig. 2c) shows values of 3–7 mm day⁻¹, with a reverse North-South pattern and underestimated precipitation south
of the Yangtze River compared to ERA Interim.

235 The seasonal cycle of precipitation in the YRV region has a precipitation mean above 5 mm day⁻¹ from April to August,
and a clear precipitation peak in June according to ERA-Interim (Fig. 3a, black dashed line). Precipitation in the CTL (red)
and PIN (blue) simulations peaks during May and June, with a marked decrease from July. Precipitation in May to June is
overestimated, while precipitation in July and August is underestimated. Taking into account inter-annual variations (shading),
the overall magnitudes and timing of mean precipitation are rather similar in the YRV region for both model runs compared
240 to ERA-Interim. However, given the coarser resolution, different parameterisations, and absence of data assimilation, a perfect
match between the climate models and reanalysis can not be expected. In addition, only limited periods of the CTL and PIN
simulations are compared to the longer reanalysis data.

In summary, the representation of summer precipitation in South Asia by the climate model simulations is slightly under-
estimated, especially in July. The PIN simulation, which has a higher resolution than CTL, correctly shows a precipitation
245 peak during June. Generally, the precipitation maximum south of the Tibetan Plateau is overestimated, while at the same time,
precipitation over South China, the Indochina Peninsula, the BoB and Western Pacific is underestimated. In particular the
precipitation differences over land should be kept in mind for the later analysis, as they can contribute to the YRV through
continental recycling of moisture from land evaporation (Fremme and Sodemann, 2019). Nonetheless, the mean precipitation
differences in the YRV are generally smaller than in the surrounding regions, providing a suitable basis for the following
250 analysis of the moisture sources in both climate model simulations.

3.2 Precipitation estimate from the WaterSip method for CTL and PIN

The above comparison of climate model precipitation with the ERA-Interim reanalysis shows the skill and shortcomings of
both climate models in representing YRV precipitation. However, as described in Sec. 2.3, the moisture sources are obtained
from specific humidity, rather than the precipitation field calculated by the climate models. From the specific humidity decrease
255 during the last time step before a trajectory end point, the WaterSip method provides an estimate of the precipitation amount,
denoted here as the Lagrangian precipitation estimate Π (in units of mm day⁻¹). Differences between this precipitation estimate
from WaterSip and the model-derived precipitation field allow us to assess the representativeness of the results from the

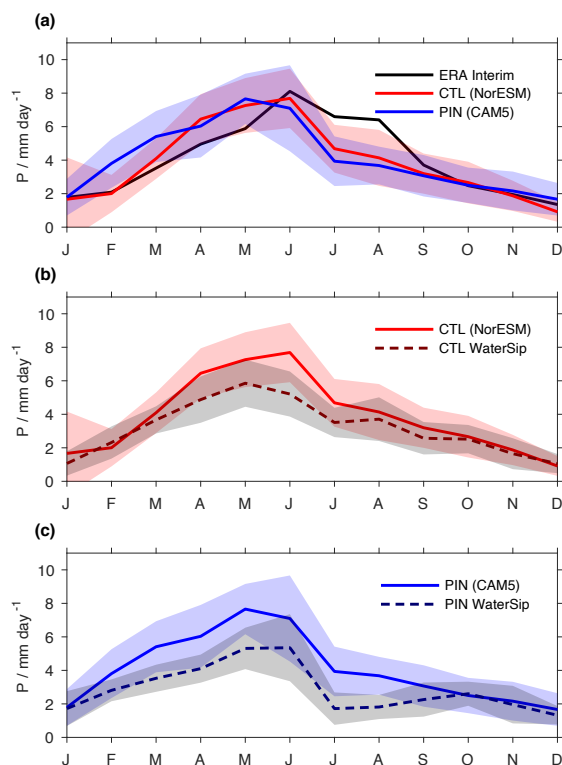


Figure 3. YRV monthly mean precipitation in the near-present time period. (a) mean precipitation seasonality for ERA Interim (black), CTL (red), and PIN (blue) in mm day^{-1} . (b) Comparison between simulated CTL precipitation in the YRV (red) and the corresponding precipitation estimate from the WaterSip diagnostic (red dashed). (c) Comparison between simulated PIN precipitation in the YRV (blue) and the corresponding precipitation estimate from the WaterSip diagnostic (blue dashed). Shaded areas indicate the inter-annual $1-\sigma$ standard deviation of the mean.

moisture source diagnostic. Past studies found that Π often has a positive bias of up to 20%, which could be due to both the neglect of microphysical processes and uncertainty from interpolation during trajectory calculations (Stohl et al., 2005; Sodemann et al., 2008; Sodemann and Zubler, 2010; Sodemann, 2020). Since it is used as a measure of consistency, the precipitation estimate Π should primarily be compared to each respective model simulation, rather than ERA-Interim.

For the CTL simulation, mean estimated precipitation (Fig. 3b, red solid line) is underestimated from April to June compared to simulated precipitation (red dashed line), with an average of 1.0 mm day^{-1} . All other months show a good correspondence, with an annual average overestimation of about 0.1 mm day^{-1} . Estimated precipitation peaks in the same month (May) as the climate model precipitation. For the PIN simulation, estimated precipitation from WaterSip (Fig. 3c, blue line) is very similar to CAM5 precipitation (blue dashed line). As for the CTL simulation, the summer precipitation is underestimated. On average, CAM5 and WaterSip-estimated precipitation differ by 0.5 mm day^{-1} , which is within the range seen in previous studies using



Lagrangian moisture source diagnostics. Note that also in terms of spatial distribution, the WaterSip-estimated precipitation is also rather similar to both CTL and PIN precipitation (not shown). The good correspondence between the precipitation estimate and climate model precipitation confirms that the choice of parameters for the moisture source diagnostic (Appendix A) allows to obtain representative insight into the moisture transport and moisture sources of precipitation in the YRV.

3.3 Moisture source locations for near-present simulations

Now we compare the moisture source locations between different climate simulations for present-day and the preindustrial period. Moisture source area maps can be interpreted as the share of total evaporation in the shaded regions that will contribute to precipitation in the target region YRV (Fig. 4, red box). These evaporation contributions, or moisture sources, are denoted here by the symbol ϵ (mm day^{-1}). The 35-year mean moisture sources obtained from ERAI during summer (MJJ) serve again as a reference in a comparison between the near-present simulations. Based on ERAI, the moisture sources pertaining to the YRV precipitation are distributed over a fairly large region, reaching across the Indian subcontinent (Fig. 4a). Note that evaporation contributions are everywhere clearly lower ($<0.9 \text{ mm day}^{-1}$, Fig. 4a) than mean precipitation ($\approx 6 \text{ mm day}^{-1}$), indicating that only a fraction of the precipitation is recycled into the YRV region. For ERAI, the source maximum is just southwest of the YRV. This region contributes with a summer average of 0.8 mm day^{-1} to YRV precipitation. The dotted contour lines denote the 50th and 80th percentiles of ϵ (Fig. 4c). The innermost dotted contour shows that 50% of the moisture comes from land regions south and southwest of the YRV and nearby ocean regions. The cyan contour shows that additional 30% of moisture comes from more distant land regions as well as parts of the Western Pacific, the south China Sea and the Bay of Bengal. Here, contributions from evaporation to YRV precipitation are generally low ($<0.2 \text{ mm day}^{-1}$), but spread out over a wide area.

At first glance, the moisture sources for CTL are quite similar to the ERAI results (Fig. 4b). Highest values are within or close to the YRV. The sources also extend further south than north, and more to the west than to the east, especially over land. However, some important differences can be seen. Moisture sources for the CTL run show a maximum contribution from a single region of $<0.9 \text{ mm day}^{-1}$ (Fig. 4b), similar to ERAI. For CTL, the 50th percentile extends less south over the Indochina peninsula than for the reference run, and the 80th percentile covers extends less to the west and south but more east. For the PIN case, the average moisture contribution from a particular region does not exceed 0.7 mm day^{-1} (Fig. 4c), which is lower than for CTL and ERAI ($<0.9 \text{ mm day}^{-1}$). The 50th percentile for PIN is similar to the CTL run, encompassing land regions to the south and southwest as well as nearby ocean regions. The 80th percentile in PIN, compared to both CTL and ERAI, is shifted from the Western Pacific towards India and into the Arabian sea compared to CTL, albeit extending less west and south than ERAI.

Comparing moisture sources for the CTL run to ERAI in more detail in terms of relative difference, it is apparent that the YRV region itself contributes slightly more in both climate models than ERAI (Fig. 4d). The largest relative differences are however located outside the YRV region. By constraining the shading to within the 80th percentiles, we focus on differences within the most relevant moisture sources regions. For the CTL simulation, evaporation contributions are higher over the South China Sea and the Western Pacific and Bangladesh (Fig. 4d). Parts of these regions contribute more than twice as much as in



ERA-Interim (ERA-I). Apart from the increased moisture source contribution from the BoB, moisture sources in CTL are shifted further to the east, compared to ERA-I.

For PIN, the most important area with increased evaporation contribution (more than 100% compared to ERA-I) are parts of the Bay of Bengal (Fig. 4e). Pacific contributions during PIN are more similar to ERA-I than the CTL simulation, and thus show only negligible differences. ϵ is 20–50% lower in PIN than in ERA-I over the Indochina Peninsula as well as over India. Both climate model runs also show larger contribution from the northern boundaries of the Tibetan Plateau, but this region contributes little to the total precipitation of the YRV.

The larger contribution of eastern sources in CTL could be due to a weaker influence by the Indian monsoon circulation on the YRV in that simulation. Such a circulation difference could explain the smaller contribution from distant western sources and the lower precipitation in summer. However, the larger contribution from the BoB does not fit to this hypothesis. Larger contributions from easterly sources could therefore also be related to a stronger influence by the North Western Pacific Subtropical High in the CTL simulation.

It should also be noted here again, as mentioned in Sec. 3.2, that the CTL simulation is about 1 K colder than ERA-I over the YRV, while PIN is similar or slightly warmer than ERA-I (Fig. 1b). The relatively low temperatures in the YRV persist throughout the entire simulation covering the 2006–2070 period, thus the comparison between simulations for CTL and RCP (see Sec. 3.6 below) will be internally consistent, but potentially influence the moisture sources during both runs.

3.4 Moisture source characteristics for near-present simulations

We now compare the seasonal cycle of several geographical, meteorological and method characteristics at the moisture sources on a monthly time scale for the CTL and PIN simulations, using ERA-I as a reference. The first characteristic is the fraction of land area at the moisture sources, weighted by the relative contribution to YRV precipitation (Fig. 5a). On average, the land fraction is close to 70% for all three simulations. During August and September, the fraction of moisture sources on land is slightly lower for CTL (50%, red) than for ERA-I (55%, black) and PIN (62%, blue). The substantially larger contribution from the Western Pacific in CTL, as noted above, appears to have a small influence on the balance between land and ocean sources during July and August (red line).

The mean source longitude and latitude of the moisture sources show a clear seasonality, albeit weaker for CTL (Fig. 5b and c). In June and July, the moisture sources are located furthest south and west in all three runs. While the mean moisture source longitude is similar in all runs, ranging between 95 to 115° E, the mean source latitude shows a clear bias compared to ERA-I (black dashed line), where the moisture sources are about 2° latitude further south than in CTL and PIN. This difference partly translate into differences of the mean moisture source distance (Fig. 5d). Here, ERA-I moisture sources are more distant than in CTL and PIN, with the largest differences apparent in February to March and August to September, when the PIN sources (1250 km) are closer than for CTL (1700 km) and ERA-I (1750 km), and in June, when the moisture sources are closer in CTL (2000 km) than in PIN (2350 km) and ERA-I (2500 km). The WaterSip diagnostic was able to attribute a markedly higher fraction of the estimated precipitation of CTL and PIN to sources than for ERA-I, in particular during May to November (Fig. 5f). The lower accounted fraction in ERA-I can be due to interpolation errors from the trajectory calculation, and a fraction

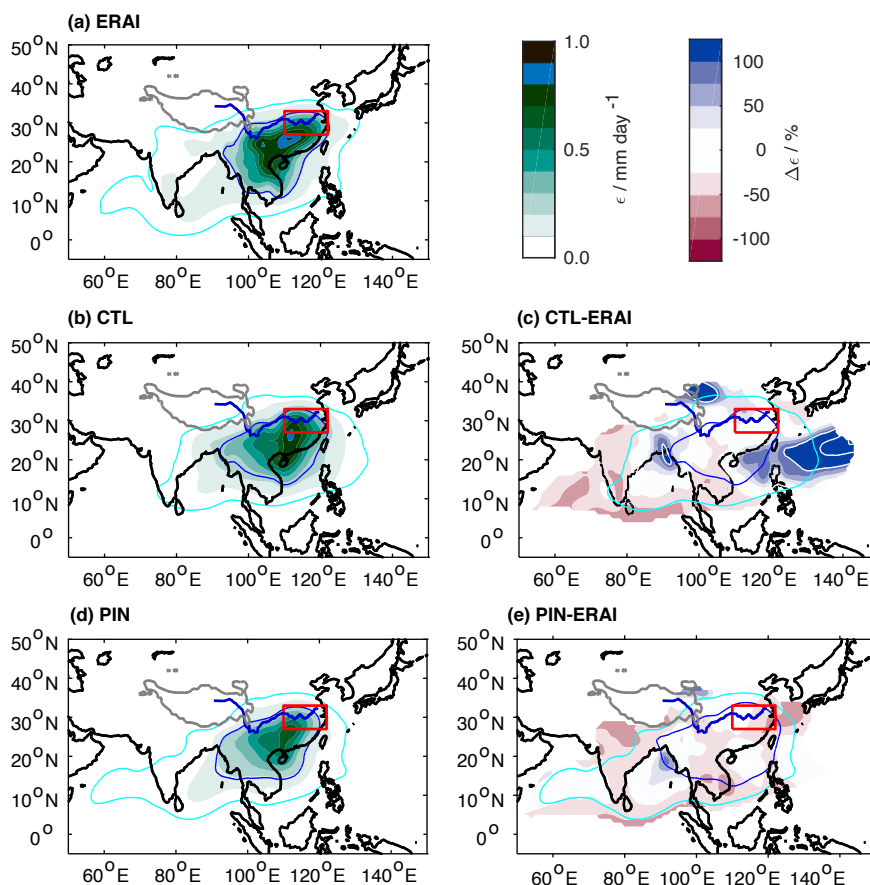


Figure 4. Comparison of summer monsoon (MJJ) moisture sources for near-present climate in the YRV. (a) Moisture source contributions ϵ_{ERAJ} (shading, mm day^{-1}) with dashed contours every 5 mm day^{-1} . (b) ϵ_{CTL} (shading, mm day^{-1}), (d) ϵ_{PIN} (shading, mm day^{-1}), (c) moisture source anomaly ($\epsilon_{\text{CTL}} - \epsilon_{\text{ERAJ}}$, %), and (e) moisture source anomaly ($\epsilon_{\text{PIN}} - \epsilon_{\text{ERAJ}}$, %). Solid contours denote the 50th (blue) and 80th percentile (cyan) of the total water mass. White contours in (c) and (e) indicate 100%. The YRV domain is outlined by a red box. The Yangtze river is denoted as a thick blue line, and elevation above 4000 m a.s.l. is indicated by a grey contour.

335 of moisture evaporated more than 15 days back in time, and, most importantly from updates to the humidity field during data assimilation.

Overall, we note a relatively high degree of consistency between the two simulations CTL and PIN, with the ERAI data set. The most substantial differences for CTL are a tendency towards more local sources and a smaller land contribution. PIN has overall very similar transport characteristics as ERAI, but a shorter monsoon season with less long-range transport.

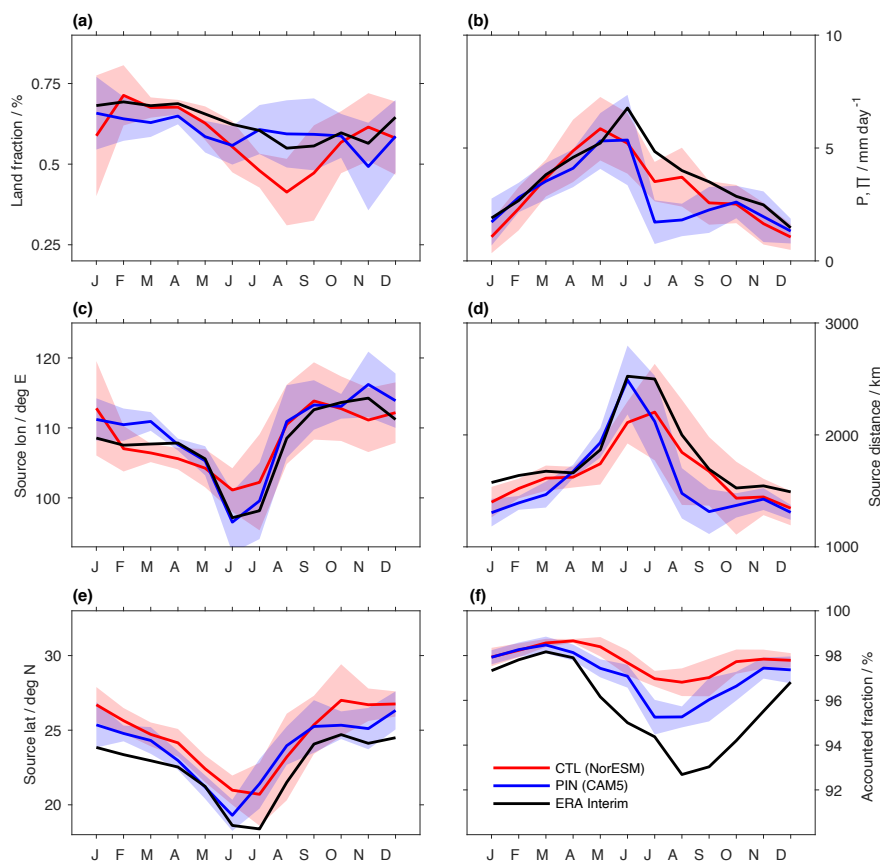


Figure 5. Seasonal mean moisture source characteristics for the YRV. (a) Land source fraction (%) for CTL (blue), PIN (red) and ERAI (black) with inter-annual 1- σ standard deviation of the mean (shading). (b) estimated precipitation amount (mm day^{-1}), (c) moisture source longitude ($^{\circ}\text{E}$), (d) moisture source distance (km), (e) moisture source latitude ($^{\circ}\text{N}$), and (f) fraction of estimated precipitation accounted for by moisture sources (%).

340 3.5 Precipitation and moisture sources in the LGM simulation

During LGM the global mean temperature was approximately 4°C colder than pre-industrial temperature (Annan and Hargreaves, 2013). In the CAM5 runs, YRV temperature is 4.0°C colder during LGM than pre-industrial (Fig. 1b). Given these temperature changes, the hydroclimate of the YRV in terms of atmospheric circulation, moisture transport and precipitation amounts can be expected to differ markedly. In previous LGM simulations, the East Asian summer monsoon has been found to
 345 be weaker as a resulting from circulation changes (Jiang and Lang, 2010). Furthermore, the precipitation response to a change in monsoon circulation strength can be expected to vary for different locations and time (Wan et al., 2011). The moisture source perspective adopted here will shed light from a different viewpoint on such expected changes.



Summer precipitation over south and east Asia in the LGM simulation from CAM5 is highest along the southern slope of the Himalayas (Fig. 6a). The LGM simulation shows lower precipitation along a belt extending from East to West the Arabian Sea, India, and the BoB compared to PIN (Fig. 6c). At the Indian west coast, LGM precipitation is more than 10 mm day⁻¹ lower than in PIN. Closer to the YRV, over South China and nearby ocean regions, LGM precipitation is up to 4 mm day⁻¹ higher than in PIN.

Summer precipitation values within the YRV region range between 5–7 mm day⁻¹ (Fig. 6a), similar to the PIN simulation. While precipitation differences in the YRV are small between LGM and PIN, a southward shift of the precipitation maximum can be noted (Fig. 6c). This southward shift is probably related to the overall precipitation increase south of the YRV in the LGM simulation. YRV precipitation from the LGM and PIN run shows that the seasonal cycle of CAM5 precipitation change little (Fig. 6e). Interestingly, LGM precipitation is higher during March, April, July and August than the PIN run, reflecting an overall broader monsoon season (Fig. 6e). The possible reasons behind this unexpected change in precipitation seasonality and length of the monsoon season are further discussed in Sec. 4.1.

The moisture sources for the LGM case show the same general features as seen for the near-present simulations (Fig. 6b). The region with highest contributions is located southwest in the YRV region, extending further in a southwesterly direction. When comparing the LGM sources with moisture sources during PIN, the strongest absolute increase can be seen over the South China Sea (Fig. 6d). Moisture sources over the Bay of Bengal also increase, whereas a decrease in ϵ can be seen over land regions west of the YRV. Comparing LGM and PIN differences as a percentage of moisture sources at each grid point underlines the change to more ocean and less land during the LGM run. Most regions show local increases in moisture contribution ϵ to the YRV of 20% and more (Fig. 6f, blue shading). The strongest increase within the 80th percentile occurs south of India, where contributions to YRV precipitation almost double compared to PIN. In contrast, land regions to the west of YRV and a part of the Western Pacific show a 20–50% decrease.

We now compare the seasonal cycle of the YRV moisture source characteristics between LGM and PIN (Fig. 7). While land fraction is overall similar for LGM and PIN, notable changes include a slightly lower land fraction in the LGM run than in PIN from June to October, and an increase in November and December (Fig. 7a). The mean moisture source position is located further South throughout the year in the LGM simulation, and during August also further East (Fig. 7b and c). These shifts in location result in more distant moisture sources during August and September (Fig. 7e). Overall, differences in LGM and PIN moisture source characteristics are remarkably small in relation to the seasonality of each characteristic during the summer monsoon, despite the pronounced temperature changes between both runs.

3.6 Precipitation and moisture sources in the RCP simulation

Next, we shift our focus to the simulations of a warmer climate. Multi-model mean CMIP5 results show a wetter East Asian monsoon region towards the end of the century under the RCP6.0 scenario, with a 7% average precipitation increase over the whole East Asian monsoon domain, and 10–15% locally over the major monsoonal front region (Seo et al., 2013). However, such a change in precipitation is not found consistently between different models (Kitoh, 2017; Yu et al., 2018).

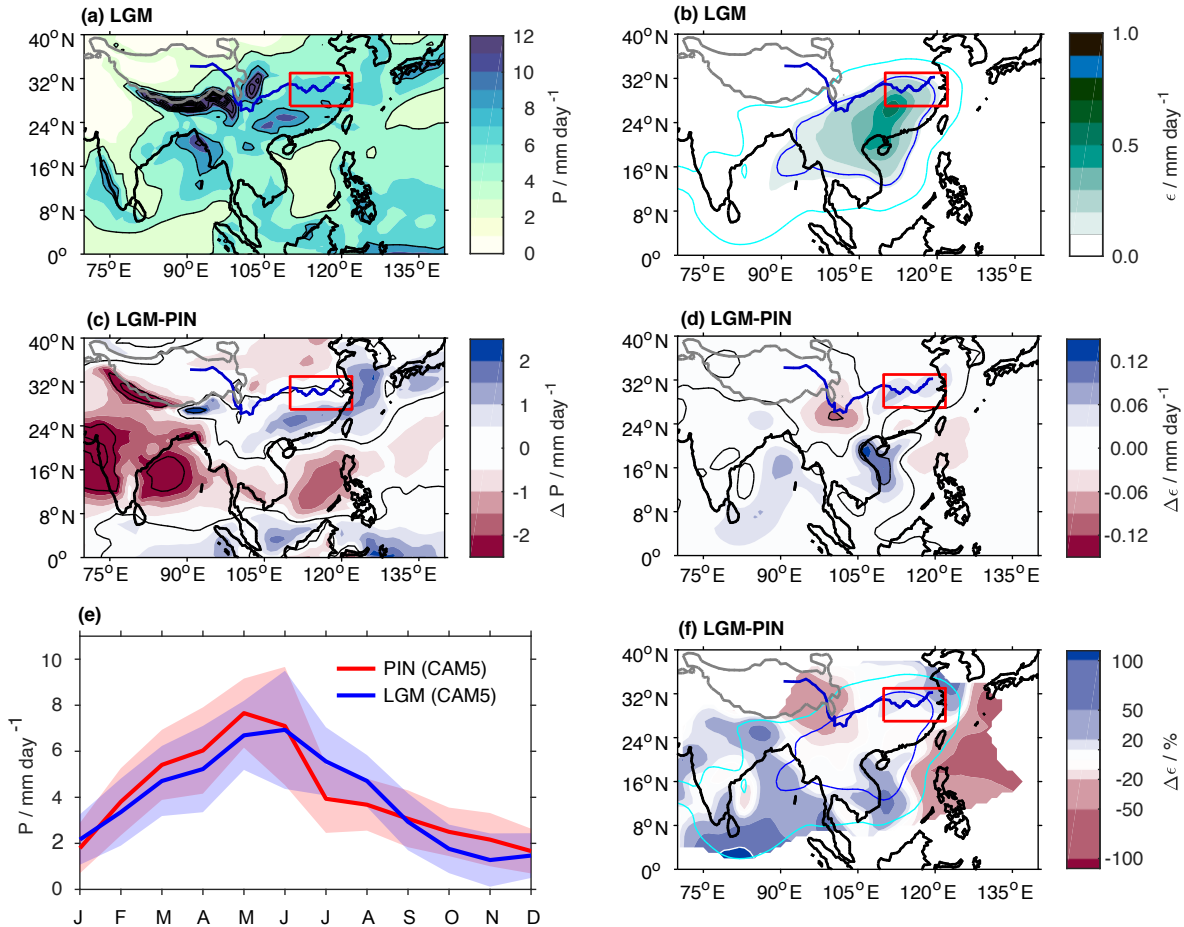


Figure 6. Precipitation and moisture source changes for the summer monsoon (MJJ) during the LGM simulation. (a) LGM precipitation mean during MJJ (shading, mm day^{-1} and contours every 5 mm day^{-1}), (b) LGM moisture source contributions (ϵ_{LGM} , shading, mm day^{-1}) for MJJ, (c) precipitation difference $P_{\text{LGM}} - P_{\text{PIN}}$ (shading, mm day^{-1} and contours every 5 mm day^{-1}) for MJJ, (d) as panel (c), but in units of % for areas where $\epsilon_{\text{PIN}} > 0.025 \text{ mm day}^{-1}$. Solid contours in (b) and (e) denote the 50th (blue) and 80th percentile (cyan) of the total water mass. The YRV region is outlined by a red square, and a thick blue contour denotes the Yangtze River.

For the future climate simulation RCP analysed here, the general picture of summer precipitation over South and East Asia shows maxima at the southern edge of the Tibetan plateau and the west coast of India, with second-order maxima over the Indochina peninsula, and the West Pacific, similar to the CTL simulation (Fig. 8a). In absolute terms, summer precipitation decreases in nearby land regions, and increases across a wide belt stretching from India to the Philippines (Fig. 8b). Interestingly, it is hardly possible to detect changes in the seasonality of monthly mean precipitation between CTL and RCP, both with respect to amount and timing (Fig. 8e).

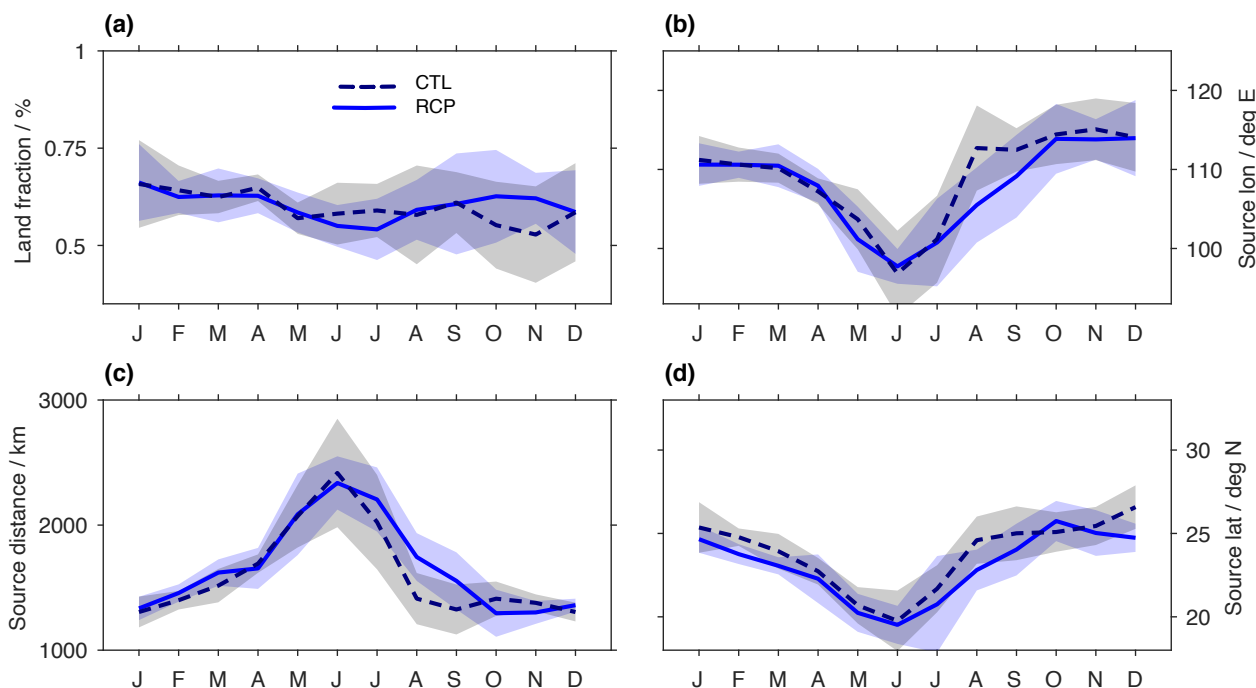


Figure 7. As Fig. 5, but for the moisture source characteristics diagnosed from the simulations LGM (blue) and PIN (black).

Moisture sources for the RCP are centered southwest of and within the YRV, similar to the CTL simulation (Fig. 8b). The largest absolute increases can be seen south of the YRV, and directly to the east towards Bangladesh (Fig. 8d). Comparing the percentage change between CTL and RCP within the 80th percentile contour further highlights the most marked differences, namely an increase of up to 50% over the ocean regions of the Western Pacific, coastal regions of the South China Sea and the Bay of Bengal towards India (Fig. 8f). The largest decreases are identified northeast of the YRV (20–50%), and over the southern BoB (20–50%).

Comparing the moisture source characteristics of the RCP run to CTL show that the 10-year climatologies remain mostly within inter-annual standard deviations (Fig. 9). Changes in contribution from moisture sources on land and ocean in the RCP run during summer appear to balance each other, leading only to a slight increase of land contribution the RCP run in the later half of the year (Fig. 9a). The most notable change can be seen for the moisture source distance (Fig. 9c). During the second half of the year (July to November), average moisture distance decreases from around 1800 km to 1500 km, indicating a stronger role of local recycling over land in the RCP run. This is also reflected in more easterly moisture source locations during RCP (Fig. 9b)

In summary, changes in simulated YRV precipitation are to first order negligible between the RCP and CTL simulations. However, the moisture source characteristics reveal underlying changes in mechanisms, pointing towards a lesser contribution of land sources during the second half of the year. Such a change could be due to circulation changes, possibly connected



to stronger continental rainout (and recycling) upstream of the YRV. The moisture sources analysis indicates that the small changes in absolute amount may be the result of a shift from more distant to more local land and ocean source regions. 405 Nonetheless, the moisture source regime in the YRV region only shows marginal changes according to our simulation with an RCP6 emission scenario until 2070. A higher emission scenario, as well as analysis of more years and different models would be useful corroborate the findings regarding the detected shifts from remote to local source contributions.

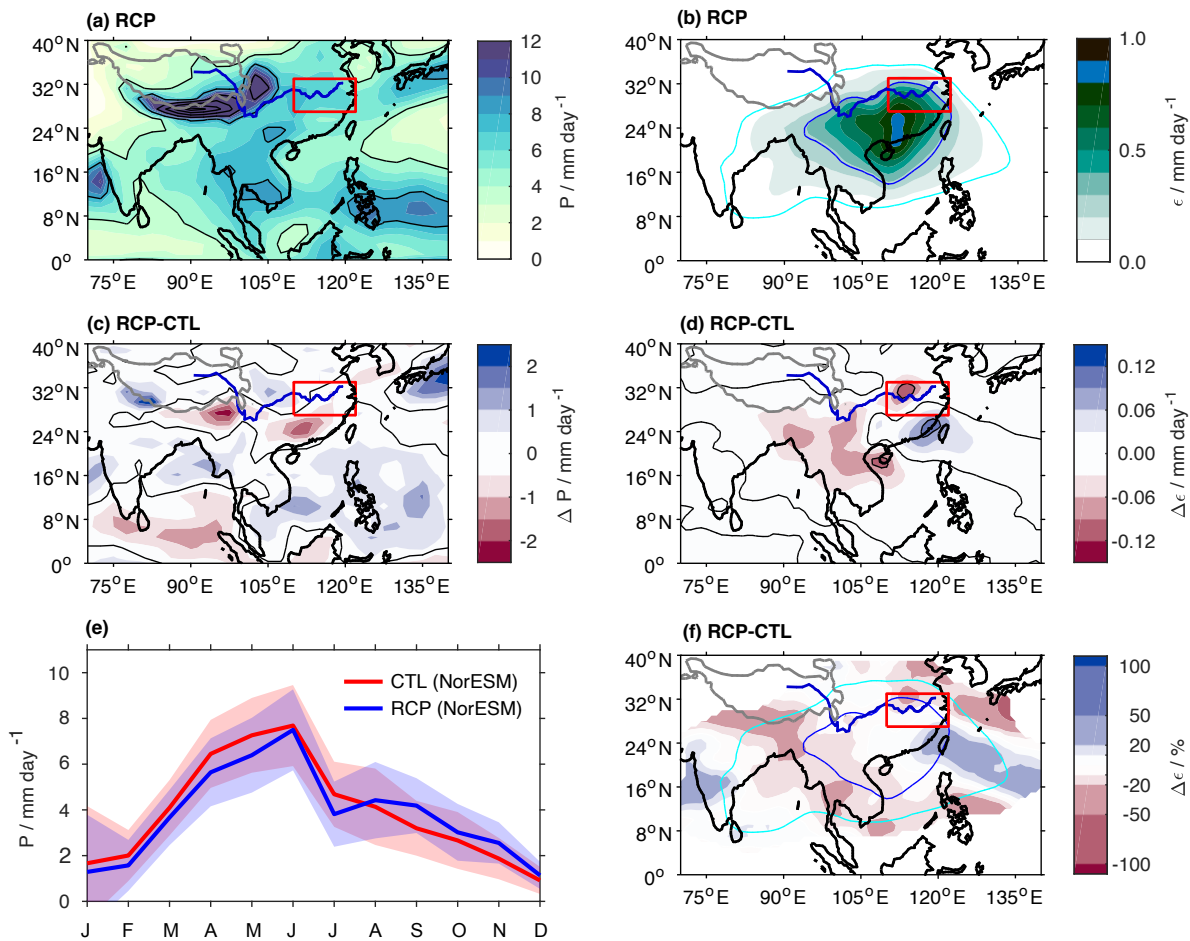


Figure 8. Precipitation and moisture source changes for the summer monsoon (MJJ) during the RCP simulation. (a) RCP precipitation mean during MJJ (shading, mm day^{-1} and contours every 5 mm day^{-1}), (b) RCP moisture source contributions (ϵ_{RCP} , shading, mm day^{-1}) for MJJ, (c) precipitation difference $P_{\text{RCP}} - P_{\text{CTL}}$ (shading, mm day^{-1} and contours every 5 mm day^{-1}) for MJJ, (d) as panel (c), but in units of % for areas where $\epsilon_{\text{CTL}} > 0.025 \text{ mm day}^{-1}$. Solid contours in (b) and (e) denote the 50th (blue) and 80th percentiles of the total water mass. The YRV region is outlined by a red square, and a thick blue contour denotes the Yangtze River.

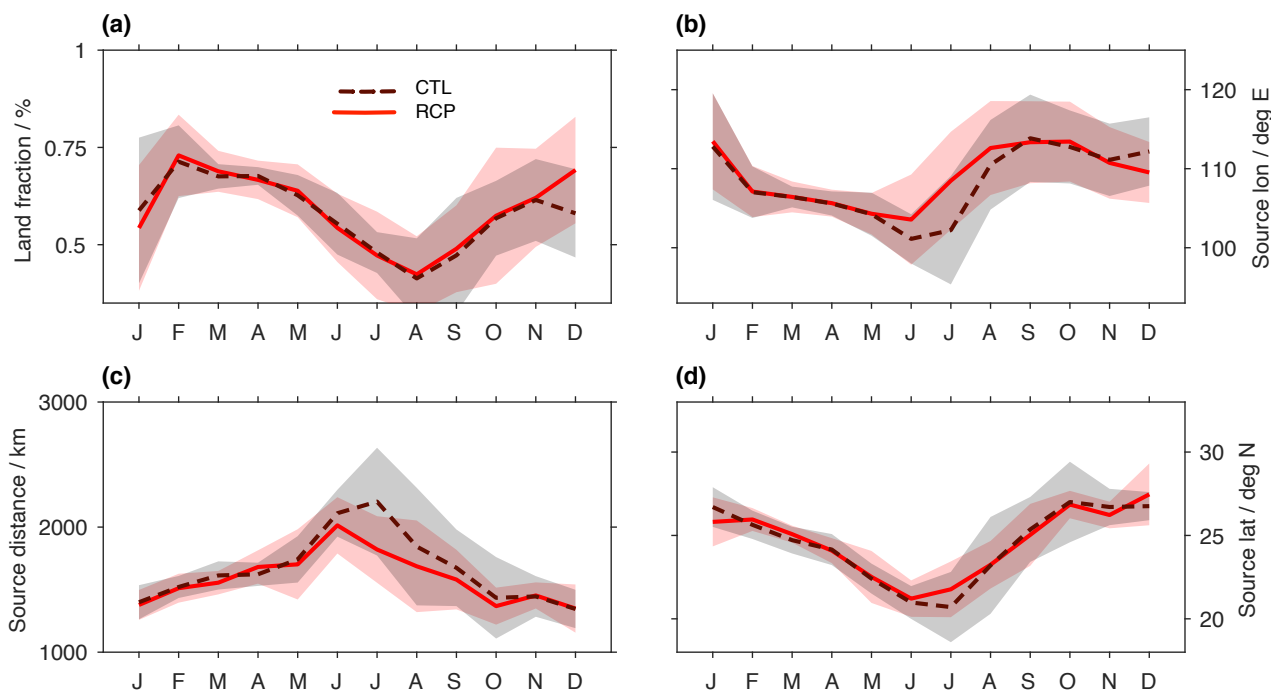


Figure 9. As Fig. 5, but for the moisture source characteristics diagnosed from the simulations CTL (dark red dashed line) and RCP (red solid line).

4 Discussion

4.1 Differences of the monsoon seasonality during the LGM

410 During the analysis of the LGM simulation (Sec. 3.5), an overall increase in the summer precipitation total, and a broader seasonality were noted (Fig. 6d). Here we explore two hypotheses that potentially could explain the simulated changes in precipitation by means of the corresponding moisture sources (Fig. 7).

A first hypothesis is that the increase in LGM precipitation in the YRV could be caused by a shift in local moisture transport pathways, specifically by increasing moisture transport from regions south of the YRV to the target area. Such a shift in
 415 atmospheric circulation can for example be caused by downstream effects of the ice sheet topography changes between PIN and the LGM simulation, or other circulation changes in response to different climate forcings. Stronger southwesterly winds could increase the moisture flux from the South China Sea, Indochina Peninsula and Bay of Bengal. The higher water vapour flux could be further amplified by more local recycling, and thus lead to a general increase in precipitation in the region.

A second hypothesis stems from the apparent opposite relation between the changes in precipitation between LGM and
 420 PIN (Fig. 6b) and the moisture contributed from those regions (Fig. 6d). More specifically, India and the surrounding oceans receive less precipitation, but contribute more as sources to YRV. Instead, the Western Pacific and West China receive more



precipitation, but contribute less as moisture sources to the YRV. This finding is most pronounced for the more remote moisture sources. A potential explanation is thus that overall colder air masses and land regions during the LGM could be less efficient in raining out the precipitation underway from India and the BoB region, and thus lead to increased moisture source contributions
425 from these regions. In other words, the changes in moisture sources could be caused by a decreased efficiency of precipitation processes, leading to transport from southwestern distant sources.

This second hypothesis is consistent with observations of seasonal variations of moisture transport over central Europe and other regions. For example, Sodemann and Zubler (2010) find that moisture sources are more distant during winter time than during summer, resulting from both changes in circulation pattern and lower evapotranspiration during the winter. Fremme
430 and Sodemann (2019) highlighted the important role of land regions south of the YRV in the summertime moisture supply during the present-day climate by repeated precipitation recycling. In a colder climate, such recycling processes, as well as the corresponding evapotranspiration are expected to weaken. Since the first hypothesis would imply stronger evaporation both for recycling and higher water vapour fluxes in the atmosphere, we consider the second hypothesis as the more plausible explanation for the observed changes from LGM to PIN.

435 4.2 Moisture sources as an indicator for hydroclimatic changes

The comparison between the moisture sources during the near present climate with LGM (Fig. 6) and the near-present with RCP (Fig. 8) showed only relatively minor changes between different climate states. Here we investigate the implications of this unexpected finding more closely. A direct comparison of the 80th-percentile contours for all near-present simulations shows that PIN has a moisture source footprint that in terms of extension and shape resembles quite closely to ERAI (Fig.10a).
440 CTL in contrast has a smaller 80th percentile footprint, in particular over the Indian Ocean, India, and the BoB. Also the 50th percentile contour of CTL extends less to the southwest compared to PIN and ERAI. When comparing in addition the LGM and RCP percentile contours, it becomes apparent that the shapes appear to be characteristic for each model (Fig.10b). In other words, the differences between different models are similarly large as the differences between different boundary conditions.

This implies that NorESM generally simulates the hydroclimate over the YRV differently than CAM5, specifically with less
445 long-range transport. Using ERAI as a reference, it appears that NorESM has a bias towards more local moisture sources of the YRV. The reasons for such a bias may have a range of different causes, such as a coupled versus a slab ocean, but would need further sensitivity studies and analysis to identify with certainty.

Finally, the strong resemblance of moisture sources for each model across boundary condition changes seems to indicate that the models respond primarily by scaling the present-day hydroclimate. More substantial circulation changes, such as
450 additional source regions, or the shift of the maximum, are not apparent in our results. This raises the question to what degree the models are in fact able to reorganise the hydroclimate. If however, the actual YRV summer monsoon primarily responds to boundary-condition changes by scaling, it would be valuable to interpret past climate records, and adapt to future climate change.

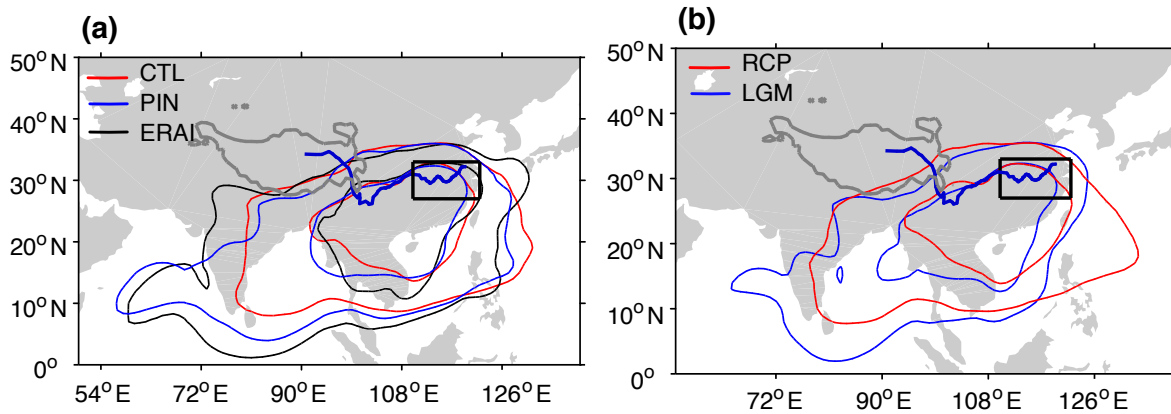


Figure 10. Comparison of moisture source changes for (a) present-day climates (CTL, dark red; PIN, dark blue; ERAI, black) and (b) past and future climate (LGM, blue; RCP, red). Lines show the 50th and 80th percentile of the MJJ mean moisture sources for each respective 10-year simulation. Black box denotes the YRV region, Yangtze river in thick blue. The grey contour denotes and elevation of 4000 m a.s.l.

5 Conclusions

455 We have investigated the changes in moisture sources and transport processes for precipitation in the Yangtze River Valley (YRV) in climate model simulations across different climates, using a quantitative Lagrangian moisture source diagnostic. The changes in the moisture source regions are different from precipitation differences between the model runs, and thus provide additional information. Thereby, we gain insight into the how the water cycle in different models responds to boundary condition changes in the East Asian summer monsoon region.

460 Comparison of a present-day control climate simulation (CTR) with a coupled NorESM, and of a pre-industrial climate simulation with an uncoupled CAM5 provide overall moisture source extend and regional contribution that is at first order very similar to the sources found for the ERA-Interim period. Land contributions from the land areas south of the YRV and over Indochina are the most important moisture source, whereas ocean areas over the Bay of Bengal (BoB) and the South China Sea and adjacent Pacific are responsible for most of the remaining contributions.

465 Also across different climate forcings, a LGM climate with CAM5, and an RCP6.0 scenario with NorESM, the general characteristics of moisture sources and moisture transport to the YRV are relatively stable for different 10-year time slices analyzed here. Moisture sources thereby remain similar with respect to the location, their magnitudes, and the relative contributions of moisture from land and ocean areas.

470 The climate model runs of the uncoupled CAM5 and the coupled NorESM for all four time slices analyzed here show slightly more local moisture origin than for the ERA-Interim simulation. This could indicate a more active land-surface interaction in terms of precipitation, turbulence and differences in the land-surface model compared to the reanalysis. Model differences could also have such an impact, for example lower resolution grid and less strong wind maxima that impact moisture transport in



the East Asian monsoon region, increased numerical diffusion of the water vapour leading to lower gradients, and to more diagnosed evaporation and precipitation events, or different representations of moist convection.

475 For the CAM5 LGM simulation, moisture sources show small differences to near-present simulation of the same climate model during summer. These differences could be caused by an increased efficiency in the moisture transport from southwestern distant sources caused by less rain-out en-route. A more detailed investigation of the respective contribution of forcing changes on the atmospheric circulation would be needed to corroborate these indicative findings.

480 For the coupled NorESM simulation using a future climate scenario with RCP6.0, the moisture sources show only small differences to the control run. Differences in the moisture source characteristics do not exceed the inter-annual standard deviation of the time slices analyzed. The small change between the moisture sources of the control and future climate could be connected to the in general limited change seen in precipitation over the East Asian monsoon region.

485 Interestingly, larger differences were seen in the moisture sources between the different climate models than between different simulations using the same model. Two interpretations of this observation are possible. If we assume the models adequately represent relevant aspects of the Earth system, our study suggests that for moderate climatic changes, the regime of moisture sources and transport in the East Asian monsoon region, in particular over the YRV, may be relatively stable, also across different climatic periods.

490 Alternatively, we can pose the question how realistic the representation of climate and of response to boundary condition changes by the different models are. It is possible that model responses are too linear, amounting primarily to the scaling of existing transport patterns and source characteristics, while it could be possible that the actual climate system allows for more drastic circulation changes result from a transition between LGM and Pre-industrial or from present-day to RCP6.0. It will be valuable to consider if certain processes indeed exert a stabilising influence on the climatic system in East Asia summer monsoon, or if models potentially miss factors and feedback that enable more substantial changes in regional climate. Comparison and interpretation with paleoclimate records of stable isotopes will be a useful asset to tie hydroclimatic model responses to observational evidence.

495 Irrespective of the answer to the cause behind muted model responses, we conclude that the moisture source perspective adopted here, that is enabled by a quantitative Lagrangian moisture source diagnostic, does provide valuable additional information that supports understanding and quantifying model responses of model hydroclimate to boundary conditions changes.

Appendix A: Sensitivity to WaterSip thresholds and time step length

500 An important advantage when diagnosing moisture sources from the NorESM simulations over the ERA-Interim reanalysis is that they are not affected by data assimilation. The absence of humidity increments from data assimilation allows us to analyze the effect of the choice of certain parameters of the WaterSip diagnostic. In this section, the effect of a change of thresholds and time step length on the moisture sources is analyzed for one year of the CTL simulation. The thresholds tested are the threshold value for the minimum change in specific humidity per time step Δq_c , the time step Δt , and the relative humidity threshold RH_c . From these threshold tests, we are able to evaluate the robustness of the overall findings presented above.



Throughout this study, the threshold for Δq_c and Δt have been set to $0.1 \text{ g kg}^{-1} \text{ h}^{-1}$ and 6 h, respectively. These parameters are the same as for the study of Fremme and Sodemann (2019) using ERAI data, thus making the results directly comparable. The specific humidity change threshold Δq_c determines the limit above which changes in specific humidity in air parcels are recorded as due to either precipitation and evaporation events. Humidity changes below the threshold are considered due to
510 interpolation errors, and are not taken into account for the moisture source diagnostic. The time steps tested here are for 3, 6, 9, and 12 hour duration, and for the specific humidity thresholds shown in Table A1.

A1 Sensitivity to specific humidity threshold changes

The effect of the specific humidity threshold change together with changes of the time step length on moisture sources becomes apparent from the mean distance of the moisture sources for YRV precipitation (Fig. A1). For comparison, the Δq_c are
515 converted to the unit $\text{g kg}^{-1} \text{ h}^{-1}$. With the setting chosen here for 6 h as a reference (red symbols), it is apparent that longer Δt result in more distant sources for the same Δq_c . The moisture source distance is approximately 300 km larger for a 6 h than for a 3 h time step. Similarly, the sensitivity runs with a 12 h time step have also about 300 km more distant source regions than the 6 h run. Long Δt can invalidate the assumption that all humidity changes in an air parcel are due to either evaporation or
520 precipitation only, and that the other process can be disregarded. While this would suggest that the 3 h time step gives the most accurate results, such short time steps can introduce larger errors as Δq_c reaches a similar magnitude as numerical noise and interpolation errors. Values of above 6 h are likely to lead to degraded trajectory calculation, and to overlooking the influence of diurnal variation. From the above discussion, it appears that the moisture source distance has an error margin of several hundred km, or on the order of 10–20%, depending on the exact parameter choice for the time step. For the same time step, changes in Δq_c give a less distant source for higher thresholds. However, threshold values above $0.1 \text{ g kg}^{-1} \text{ h}^{-1}$ are hardly
525 typical, and only include very strong evaporation and precipitation events. For Δq_c below $0.1 \text{ g kg}^{-1} \text{ h}^{-1}$, the source distance is much less sensitive to the threshold value than to the time step.

A2 Sensitivity to relative humidity threshold changes

The relative humidity threshold RH_c is another influential parameter of the moisture source diagnostics. RH_c sets the minimum RH at which a moisture decrease within the target region is considered as a precipitation event. Therefore, RH_c has a large effect
530 on the precipitation estimated by the WaterSip method. However, RH_c can also affect the moisture sources, as the weight of individual uptakes corresponds to estimated precipitation in the target region. Throughout this study, we use a threshold value of $\text{RH}_c = 80\%$. In the sensitivity tests discussed in this section, the effect varying the RH_c between of 0–100% is tested. Note that we thereby only consider the results using RH_c between 70–90% as physically consistent with the model parameterizations.

We evaluate the effect of the RH_c changes with respect to the impact on the precipitation estimate for the target region, and the moisture source distance. As expected, a more restrictive, higher, RH_c leads to a lower precipitation estimate for the
535 target region (Fig. A2a). A change of RH_c from 80% to 70% and to 90% lead to a change in the all-year precipitation mean (3.2 mm day^{-1}) by +32% and –43% respectively. The value of $\text{RH}_c = 80\%$ used throughout this study gives the precipitation estimate closest to the all-year mean precipitation from NorESM.



Changes in precipitation with changing RH_c are accompanied by change in source distance (Fig. A2b). When RH_c is changed
540 from 80% to either 70% or 90%, the mean source distance changes from an average of 1740 km by only -5% and 4% ,
respectively. Even with a more extreme change in the RH_c to as much as 30%, source distance only changes by around 20%
compared to $RH_c = 90\%$.

The small changes in source distance suggests that the RH_c only has a minor impact on the moisture source results presented
here, and leads to a uniform scaling of the moisture sources, rather than a shift. Therefore, we do not find a need to modify
545 the RH_c of 80%, in particular as the precipitation estimated by WaterSip follows the original climate model precipitation
reasonably well (Fig. 3). We conclude from this sensitivity study that the moisture source results are overall robust regarding
specific parameter changes within physical reasonable limits. This finding confirms the sensitivity experiments of the same
method by Läderach and Sodemann (2016) based on ERAI data.

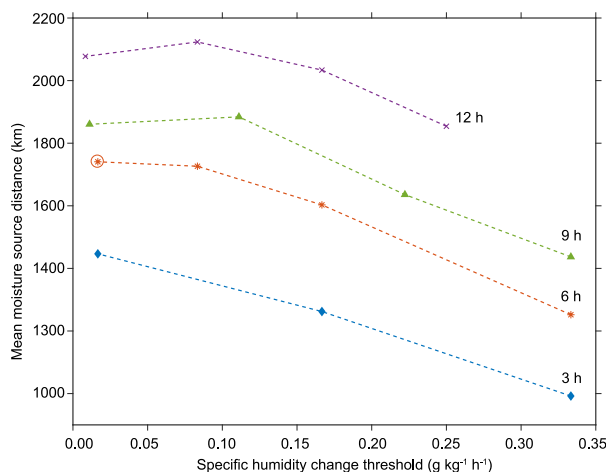


Figure A1. Sensitivity of the moisture source distance with respect to changes in the specific humidity threshold (Δq_c) and time step (Δt) for a range of 3 to 12 h. Markers denote the average distance from moisture source to the target region in km. All sensitivity runs were done for the year 2002 of the CTL simulation.

Competing interests. The authors declare no competing interests.

550 *Acknowledgements.* This work was supported by the project UTF-2016-long-term/10030 and the Swiss National Science Foundation through grant No. 200021_143436 "Spatial and Temporal Scales of Linkages in the Atmospheric Water Cycle (Waterscales)2. This work used storage capacity from the Norwegian computing infrastructure Sigma2 through project NS9054K (COPEWET) and NS2345K (EVA). Access to the ECMWF ERA-Interim reanalysis data was provided through Met Norway. This work has been supported by the Research Council of Norway through the project EVA (grant no. 229771).

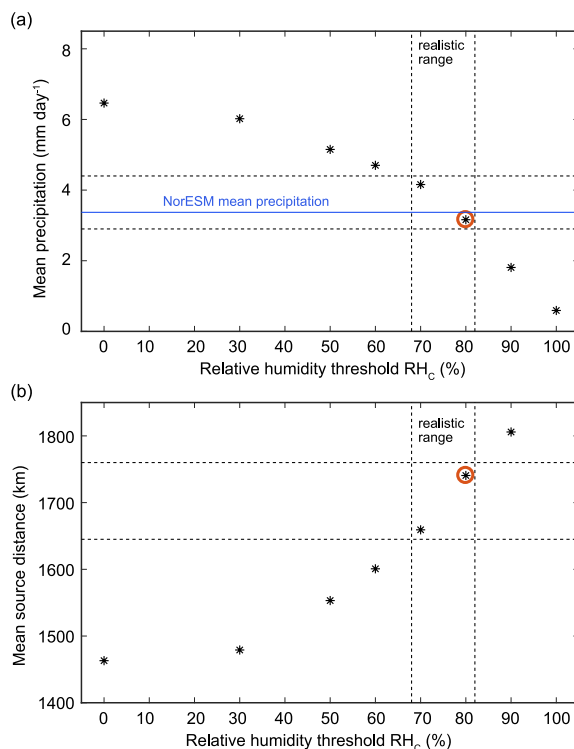


Figure A2. Sensitivity of the precipitation estimate and moisture source distance to changes in the relative humidity threshold (RH_c). (a) Sensitivity of the precipitation estimate (mm day^{-1}) in response to RH_c . Anticipated realistic range of P indicated by dashed lines. Blue line shows precipitation simulated by NorESM1-M. (b) Response of moisture source distance (km) to changes in RH_c . Value for threshold RH_c adopted in this study is highlighted by a red circle. All sensitivity runs are based on the year 2002 of the CTL simulation.

Table A1. Range of parameters for the sensitivity tests, including the time steps Δt , specific humidity thresholds Δq_c , and the relative humidity threshold RH_c . Numbers in brackets for Δq_c are in units of $\text{g kg}^{-1}\text{h}^{-1}$ for easier comparison.

Time step length	Specific humidity thresholds (g kg^{-1})					
3 h	0.05 (0.0167)	0.5 (0.167)	1.0 (0.333)			
6 h	0.1 (0.0167)	0.5 (0.083)	1.0 (0.167)	2.0 (0.667)		
9 h	0.1 (0.0111)	1.0 (0.111)	2.0 (0.222)	3.0 (0.333)		
12 h	0.1 (0.008)	1.0 (0.083)	2.0 (0.167)	3.0 (0.250)		
Relative humidity thresholds (%)						
0	30	50	60	70	80	90



555 References

- Abe-Ouchi, A., Saito, F., Kageyama, M., Braconnot, P., Harrison, S. P., Lambeck, K., Otto-Bliesner, B. L., Peltier, W. R., Tarasov, L., Peterschmitt, J. Y., and Takahashi, K.: Ice-sheet configuration in the CMIP5/PMIP3 Last Glacial Maximum experiments, *Geoscientific Model Development*, 8, 3621–3637, <https://doi.org/10.5194/gmd-8-3621-2015>, 2015.
- Annan, J. D. and Hargreaves, J. C.: A new global reconstruction of temperature changes at the Last Glacial Maximum, *Climate of the Past*, 560 9, 367–376, <https://doi.org/10.5194/cp-9-367-2013>, 2013.
- Ashfaq, M., Rastogi, D., Mei, R., Touma, D., and Ruby Leung, L.: Sources of errors in the simulation of south Asian summer monsoon in the CMIP5 GCMs, *Climate Dynamics*, 49, 193–223, <https://doi.org/10.1007/s00382-016-3337-7>, 2017.
- Baker, A., Sodemann, H., Baldini, J., Breitenbach, S., Johnson, K., van Hunen, J., and Zhang, P.: Seasonality of westerly moisture transport in the East Asian summer monsoon and its implications for interpreting precipitation $\delta^{18}\text{O}$, *Journal of Geophysical Research: Atmospheres*, 565 120, 5850–5862, <https://doi.org/10.1002/2014JD022919>, 2015.
- Bentsen, M., Bethke, I., Debernard, J. B., Iversen, T., Kirkevåg, A., Seland, O., Drange, H., Roelandt, C., Seierstad, I. A., Hoose, C., and Kristjansson, J. E.: The Norwegian Earth System Model, NorESM1-M - Part 1: Description and basic evaluation of the physical climate, *Geoscientific Model Development*, 6, 687–720, <https://doi.org/10.5194/gmd-6-687-2013>, 2013.
- Bohlinger, P., Sorteberg, A., and Sodemann, H.: Synoptic Conditions and Moisture Sources Actuating Extreme Precipitation in Nepal, *Journal of Geophysical Research: Atmospheres*, 570 <https://doi.org/10.1002/2017JD027543>, 2017.
- Braconnot, P., Harrison, S. P., Kageyama, M., Bartlein, P. J., Masson-Delmotte, V., Abe-Ouchi, A., Otto-Bliesner, B., and Zhao, Y.: Evaluation of climate models using palaeoclimatic data, *Nature Climate Change*, 2, 417–424, <https://doi.org/10.1038/nclimate1456>, 2012.
- Cassiani, M., Stohl, A., Olivie, D., Seland, Ø., Bethke, I., Pisso, I., and Iversen, T.: The offline Lagrangian particle model FLEXPART-NorESM/CAM (v1): Model description and comparisons with the online NorESM transport scheme and with the reference FLEXPART model, *Geoscientific Model Development*, 9, 4029–4048, <https://doi.org/10.5194/gmd-9-4029-2016>, 2016.
- Chen, B., Xu, X.-D., and Zhao, T.: Main moisture sources affecting lower Yangtze River Basin in boreal summers during 2004–2009, *International Journal of Climatology*, 33, 1035–1046, <https://doi.org/10.1002/joc.3495>, 2013.
- Dee, D. P., Uppala, S. M., Simmons, A. J., Berrisford, P., Poli, P., Kobayashi, S., Andrae, U., Balmaseda, M. A., Balsamo, G., Bauer, P., Bechtold, P., Beljaars, A. C. M., van de Berg, L., Bidlot, J., Bormann, N., Delsol, C., Dragani, R., Fuentes, M., Geer, A. J., Haimberger, L., Healy, S. B., Hersbach, H., Holm, E. V., Isaksen, L., Kallberg, P., Kohler, M., Matricardi, M., McNally, A. P., Monge-Sanz, B. M., Morcrette, J. J., Park, B. K., Peubey, C., de Rosnay, P., Tavolato, C., Thepaut, J. N., and Vitart, F.: The ERA-Interim reanalysis: configuration and performance of the data assimilation system, *Quarterly Journal of the Royal Meteorological Society*, 137, 553–597, <https://doi.org/10.1002/qj.828>, 2011.
- Dykoski, C. A., Edwards, R. L., Cheng, H., Yuan, D. X., Cai, Y. J., Zhang, M. L., Lin, Y. S., Qing, J. M., An, Z. S., and Revenaugh, J.: A high-resolution, absolute-dated Holocene and deglacial Asian monsoon record from Dongge Cave, China, *Earth and Planetary Science Letters*, 233, 71–86, <https://doi.org/10.1016/j.epsl.2005.01.036>, 2005.
- Fremme, A. and Sodemann, H.: The role of land and ocean evaporation on the variability of precipitation in the Yangtze River Valley, *Hydrology and Earth System Sciences*, (accepted for publication 26.04.2019), <https://doi.org/10.5194/hess-2018-629>, 2019.
- Gent, P. R., Danabasoglu, G., Donner, L. J., Holland, M. M., Hunke, E. C., Jayne, S. R., Lawrence, D. M., Neale, R. B., Rasch, P. J., Vertenstein, M., Worley, P. H., Yang, Z. L., and Zhang, M.: The community climate system model version 4, *Journal of Climate*, 24, 4973–4991, <https://doi.org/10.1175/2011JCLI4083.1>, 2011.



- Gimeno, L., Eiras-Barca, J., Durán-Quesada, A.M., Dominguez, F., van der Ent, R., Sodemann, H., Sánchez-Murillo, R., Nieto, R. and Kirchner, J. W.: The residence time of water vapour in the atmosphere., *Nat. Rev. Earth Environ.*, 2, 558–569, <https://doi.org/10.1038/s43017-021-00181-9>, 2021.
- 595 Hoyos, C. D. and Webster, P. J.: The role of intraseasonal variability in the nature of Asian monsoon precipitation, *Journal of Climate*, 20, 4402–4424, <https://doi.org/10.1175/JCLI4252.1>, 2007.
- Hu, C., Henderson, G. M., Huang, J., Xie, S., Sun, Y., and Johnson, K. R.: Quantification of Holocene Asian monsoon rainfall from spatially separated cave records, *Earth and Planetary Science Letters*, 266, 221–232, <https://doi.org/10.1016/j.epsl.2007.10.015>, 2008.
- Huang, D. Q., Zhu, J., Zhang, Y. C., Huang, Y., and Kuang, X. Y.: Assessment of summer monsoon precipitation derived from five reanalysis datasets over East Asia, *Quarterly Journal of the Royal Meteorological Society*, 142, 108–119, <https://doi.org/10.1002/qj.2634>, 2016.
- 600 Hurrell, J. W., Holland, M., Gent, P. R., Ghan, S., Kay, J. E., Kushner, P. J., Lamarque, J.-F., Large, W., Lawrence, D., Lindsay, K., Lipscomb, W. H., Long, M. C., Mahowald, N., Marsh, D. R., Neale, R. B., Rasch, P., Vavrus, S., Vertenstein, M., Bader, D., Collins, W., Hack, J., Kiehl, J., and Marshall, S.: The Community Earth System Model: A Framework for Collaborative Research, *Bulletin of the American Meteorological Society*, p. 130204122247009, <https://doi.org/10.1175/bams-d-12-00121>, 2013.
- 605 Jiang, D. and Lang, X.: Last glacial maximum East Asian monsoon: Results of PMIP simulations, *Journal of Climate*, 23, 5030–5038, <https://doi.org/10.1175/2010JCLI3526.1>, 2010.
- Kirkevåg, A., Iversen, T., Seland, Ø., Hoose, C., Kristjánsson, J. E., Struthers, H., Ekman, A. M. L., Ghan, S., Griesfeller, J., Nilsson, E. D., and Schulz, M.: Aerosol–climate interactions in the Norwegian Earth System Model – NorESM1-M, *Geoscientific Model Development*, 6, 207–244, <https://doi.org/10.5194/gmd-6-207-2013>, 2013.
- 610 Kitoh, A.: The Asian Monsoon and its Future Change in Climate Models: A Review, *Journal of the Meteorological Society of Japan. Ser. II*, 95, 7–33, <https://doi.org/10.2151/jmsj.2017-002>, 2017.
- Läderach, A. and Sodemann, H.: A revised picture of the atmospheric moisture residence time, *Geophysical Research Letters*, 43, 924–933, <https://doi.org/10.1002/2015GL067449>, 2016.
- Lamarque, J. F., Bond, T. C., Eyring, V., Granier, C., Heil, A., Klimont, Z., Lee, D., Liou, C., Mieville, A., Owen, B., Schultz, M. G., Shindell, D., Smith, S. J., Stehfest, E., Van Aardenne, J., Cooper, O. R., Kainuma, M., Mahowald, N., McConnell, J. R., Naik, V., Riahi, K., and Van Vuuren, D. P.: Historical (1850–2000) gridded anthropogenic and biomass burning emissions of reactive gases and aerosols: Methodology and application, *Atmospheric Chemistry and Physics*, 10, 7017–7039, <https://doi.org/10.5194/acp-10-7017-2010>, 2010.
- Lavers, D. A. and Villarini, G.: The nexus between atmospheric rivers and extreme precipitation across Europe, *Geophysical Research Letters*, 40, 3259–3264, <https://doi.org/10.1002/grl.50636>, 2013.
- 620 Lawrence, D. M., Oleson, K. W., Flanner, M. G., Thornton, P. E., Swenson, S. C., Lawrence, P. J., Zeng, X., Yang, Z.-L., Levis, S., Sakaguchi, K., Conan, G. B., and Slater, A. G.: No Title, *J. Adv. Model. Earth Syst.*, <https://doi.org/10.1029/2011MS000045>, 2011.
- Lin, R., Zhou, T., and Qian, Y.: Evaluation of Global Monsoon Precipitation Changes based on Five Reanalysis Datasets, *Journal of Climate*, 27, 1271–1289, <https://doi.org/10.1175/JCLI-D-13-00215.1>, 2014.
- Liu, Z., Wen, X., Brady, E. C., Otto-Bliesner, B., Yu, G., Lu, H., Cheng, H., Wang, Y., Zheng, W., Ding, Y., Edwards, R. L., Cheng, J., Liu, W., and Yang, H.: Chinese cave records and the East Asia Summer Monsoon, *Quaternary Science Reviews*, 83, 115–128, <https://doi.org/10.1016/j.quascirev.2013.10.021>, 2014.
- 625 Maher, B. A. and Thompson, R.: Oxygen isotopes from Chinese caves: records not of monsoon rainfall but of circulation regime, *Journal of Quaternary Science*, 27, 615–624, <https://doi.org/10.1002/jqs.2553>, 2012.



- 630 Neale, R. B., Gettelman, A., Park, S., Chen, C.-c., Lauritzen, P. H., Williamson, D. L., Conley, A. J., Kinnison, D., Marsh, D., Smith, A. K.,
Vitt, F., Garcia, R., Lamarque, J.-f., Mills, M., Tilmes, S., Morrison, H., Cameron-smith, P., Collins, W. D., Iacono, M. J., Easter, R. C.,
Liu, X., Ghan, S. J., Rasch, P. J., and Taylor, M. A.: Description of theNCARCommunity Atmosphere Model (CAM5), NCAR Technical
Note NCAR/TN-486+STR, 2012.
- 635 Pisso, I., Sollum, E., Grythe, H., Kristiansen, N., Cassiani, M., Eckhardt, S., Arnold, D., Morton, D., Thompson, R. L., Groot Zwaafink,
C. D., Evangeliou, N., Sodemann, H., Haimberger, L., Henne, S., Brunner, D., Burkhart, J. F., Fouilloux, A., Brioude, J., Philipp, A., Seib-
ert, P., and Stohl, A.: The Lagrangian particle dispersion model FLEXPART version 10.3, Geoscientific Model Development Discussions,
<https://doi.org/10.5194/gmd-2018-333>, 2019.
- Seo, K., Ok, J., Son, J., and Cha, D.: Assessing Future Changes in the East Asian Summer Monsoon Using CMIP5 Coupled Models, *Journal
of Climate*, 26, 7662–7675, <https://doi.org/10.1175/JCLI-D-12-00694.1>, 2013.
- Sodemann, H. and Zubler, E.: Seasonal and inter-annual variability of the moisture sources for Alpine precipitation during 1995-2002,
640 *International Journal of Climatology*, 30, 947–961, <https://doi.org/10.1002/joc.1932>, 2010.
- Sodemann, H., Schwierz, C., and Wernli, H.: Interannual variability of Greenland winter precipitation sources: Lagrangian moisture diagnos-
tic and North Atlantic Oscillation influence, *Journal of Geophysical Research-Atmospheres*, 113, <https://doi.org/10.1029/2007jd008503>,
2008.
- Sodemann, H.: Beyond turnover time: Constraining the lifetime distribution of water vapor from simple and complex approaches, *J. Climate*,
645 77 (2), 413-433, <https://doi.org/10.1175/JAS-D-18-0336.1>, 2020.
- Stohl, A., Forster, C., Frank, A., Seibert, P., and Wotawa, G.: Technical note: The Lagrangian particle dispersion model FLEXPART version
6.2, *Atmospheric Chemistry and Physics*, 5, 2461–2474, <https://doi.org/10.5194/acp-5-2461-2005>, 2005.
- Stohl, A., Forster, C., and Sodemann, H.: Remote sources of water vapor forming precipitation on the Norwegian west coast at 60N - A tale
of hurricanes and an atmospheric river, *Journal of Geophysical Research Atmospheres*, 113, 1–13, <https://doi.org/10.1029/2007JD009006>,
650 2008.
- Stohl, A., Aamaas, B., Amann, M., Baker, L. H., Bellouin, N., Berntsen, T. K., Boucher, O., Cherian, R., Collins, W., Daskalakis, N.,
Dusinska, M., Eckhardt, S., Fuglestedt, J. S., Harju, M., Heyes, C., Hodnebrog, Hao, J., Im, U., Kanakidou, M., Klimont, Z., Kupiainen,
K., Law, K. S., Lund, M. T., Maas, R., MacIntosh, C. R., Myhre, G., Myriokefalitakis, S., Olivie, D., Quaas, J., Quennehen, B., Raut, J. C.,
Rumbold, S. T., Samset, B. H., Schulz, M., Seland, Shine, K. P., Skeie, R. B., Wang, S., Yttri, K. E., and Zhu, T.: Evaluating the climate
655 and air quality impacts of short-lived pollutants, *Atmospheric Chemistry and Physics*, 15, 10 529–10 566, <https://doi.org/10.5194/acp-15-10529-2015>, 2015.
- Sun, B. and Wang, H.: Analysis of the major atmospheric moisture sources affecting three sub-regions of East China, *International Journal
of Climatology*, 35, 2243–2257, <https://doi.org/10.1002/joc.4145>, 2015.
- Taylor, K. E., Stouffer, R. J., and Meehl, G. A.: An overview of CMIP5 and the experiment design, *Bulletin of the American Meteorological
660 Society*, 93, 485–498, <https://doi.org/10.1175/BAMS-D-11-00094.1>, 2012.
- Thompson, L. G., Yao, T., Mosley-Thompson, E., Davis, M. E., Henderson, K. A., and Lin, P. N.: A high-resolution millennial record of the
South Asian Monsoon from Himalayan ice cores, *Science*, 289, 1916–1919, <https://doi.org/10.1126/science.289.5486.1916>, 2000.
- Wan, N. J., Li, H. C., Liu, Z. Q., Yang, H. Y., Yuan, D. X., and Chen, Y. H.: Spatial variations of monsoonal rain in eastern China: Instrumental,
historic and speleothem records, *Journal of Asian Earth Sciences*, 40, 1139–1150, <https://doi.org/10.1016/j.jseas.2010.10.003>, 2011.



- 665 Wang, N., Zeng, X. M., Guo, W. D., Chen, C., You, W., Zheng, Y., and Zhu, J.: Quantitative diagnosis of moisture sources and transport pathways for summer precipitation over the mid-lower Yangtze River Basin, *Journal of Hydrology*, 559, 252–265, <https://doi.org/10.1016/j.jhydrol.2018.02.003>, 2018.
- Wang, P. X., Wang, B., Cheng, H., Fasullo, J., Guo, Z. T., Kiefer, T., and Liu, Z. Y.: The global monsoon across time scales: Mechanisms and outstanding issues, *Earth-Science Reviews*, 174, 84–121, <https://doi.org/10.1016/j.earscirev.2017.07.006>, 2017.
- 670 Wang, Y. J., Cheng, H., Edwards, R. L., An, Z. S., Wu, J. Y., Shen, C. C., and Dorale, J. A.: A high-resolution absolute-dated Late Pleistocene monsoon record from Hulu Cave, China, *Science*, 294, 2345–2348, <https://doi.org/10.1126/science.1064618>, 2001.
- Webster, P. J., Magana, V. O., Palmer, T. N., Shukla, J., Tomas, R. A., Yanai, M., and Yasunari, T.: Monsoons: Processes, predictability, and the prospects for prediction, *Journal of Geophysical Research-Oceans*, 103, 14 451–14 510, <https://doi.org/10.1029/97jc02719>, 1998.
- Wei, J., Dirmeyer, P. A., Bosilovich, M. G., and Wu, R.: Water vapor sources for Yangtze River Valley rainfall: Climatology, variability, and
675 implications for rainfall forecasting, *Journal of Geophysical Research-Atmospheres*, 117, <https://doi.org/10.1029/2011JD016902>, 2012.
- Yu, Z., Gu, H., Wang, J., Xia, J., and Lu, B.: Effect of projected climate change on the hydrological regime of the Yangtze River Basin, China, *Stochastic Environmental Research and Risk Assessment*, 32, 1–16, <https://doi.org/10.1007/s00477-017-1391-2>, 2018.
- Zhou, T. J. and Yu, R. C.: Atmospheric water vapor transport associated with typical anomalous summer rainfall patterns in China, *Journal of Geophysical Research-Atmospheres*, 110, <https://doi.org/10.1029/2004JD005413>, 2005.
- 680 Zong, Y. and Chen, X.: The 1998 flood on the Yangtze, China, *Natural Hazards*, 22, 165–184, <https://doi.org/10.1023/A:1008119805106>, 2000.